AGU PUBLICATIONS

JGR

Journal of Geophysical Research: Atmospheres

RESEARCH ARTICLE

10.1002/2016JD026121

Key Points:
- Global chemistry climate models (CCMs) underestimate observed HCHO in the tropical western Pacific troposphere during CONTRAST by between 4 and 50%
- Errors in NO_x chemistry and emissions are significant drivers of the measurement versus model discrepancy for HCHO in the CCMs
- Lack of oceanic emissions and missing in situ production of acetaldehyde leads to additional global chemistry model underestimates of HCHO

Supporting Information:
- Supporting Information S1

Correspondence to:
D. C. Anderson,
danders2@umd.edu

Citation:
Anderson, D. C., Nicely, J. M., Wolfe, G. M., Hanisco, T. F., Salawitch, R. J., Canty, T. P., … Zeng, G. (2017). Formaldehyde in the tropical western Pacific: Chemical sources and sinks, convective transport, and representation in CAM-Chem and the CCMI models. *Journal of Geophysical Research: Atmospheres*, *122*, 11,201–11,226. https://doi.org/10.1002/2016JD026121

Received 20 OCT 2016
Accepted 3 OCT 2017
Accepted article online 6 OCT 2017
Published online 26 OCT 2017

©2017. American Geophysical Union. All Rights Reserved.

Formaldehyde in the Tropical Western Pacific: Chemical Sources and Sinks, Convective Transport, and Representation in CAM-Chem and the CCMI Models

Daniel C. Anderson[1], Julie M. Nicely[2,3], Glenn M. Wolfe[2,4], Thomas F. Hanisco[2], Ross J. Salawitch[1,5,6], Timothy P. Canty[1], Russell R. Dickerson[1], Eric C. Apel[7], Sunil Baidar[8,9], Thomas J. Bannan[10], Nicola J. Blake[11], Dexian Chen[12], Barbara Dix[8], Rafael P. Fernandez[13,14], Samuel R. Hall[7], Rebecca S. Hornbrook[7], L. Gregory Huey[12], Beatrice Josse[15], Patrick Jöckel[16], Douglas E. Kinnison[7], Theodore K. Koenig[8,9], Michael Le Breton[17], Virginie Marécal[15], Olaf Morgenstern[18], Luke D. Oman[2], Laura L. Pan[7], Carl Percival[10], David Plummer[19], Laura E. Revell[20,21], Eugene Rozanov[21,22], Alfonso Saiz-Lopez[13], Andrea Stenke[21], Kengo Sudo[23,24], Simone Tilmes[7], Kirk Ullmann[7], Rainer Volkamer[8,9], Andrew J. Weinheimer[7], and Guang Zeng[18]

[1]Department of Atmospheric and Oceanic Science, University of Maryland, College Park, MD, USA, [2]Atmospheric Chemistry and Dynamics Laboratory, NASA Goddard Space Flight Center, Greenbelt, MD, USA, [3]Universities Space Research Association, Columbia, MD, USA, [4]Joint Center for Earth Systems Technology, University of Maryland, Baltimore County, Baltimore, MD, USA, [5]Earth System Science Interdisciplinary Center, University of Maryland, College Park, MD, USA, [6]Department of Chemistry and Biochemistry, University of Maryland, College Park, MD, USA, [7]National Center for Atmospheric Research, Boulder, CO, USA, [8]Department of Chemistry, University of Colorado Boulder, Boulder, CO, USA, [9]Cooperative Institute for Research in Environmental Sciences, Boulder, CO, USA, [10]Department of Chemistry, University of Manchester, Manchester, UK, [11]Department of Chemistry, University of California, Irvine, CA, USA, [12]School of Earth and Atmospheric Sciences, Georgia Institute of Technology, Atlanta, GA, USA, [13]Department of Atmospheric Chemistry and Climate, Institute of Physical Chemistry Rocasolano, CSIC, Madrid, Spain, [14]Department of Natural Science, National Research Council (CONICET), FCEN-UNCuyo, Mendoza, Argentina, [15]Centre National de Recherche Météorologique, UMR3589, Météo-France-CNRS, Toulouse, France, [16]Deutsches Zentrum für Luft- und Raumfahrt, Institut für Physik der Atmosphäre, Oberpfaffenhofen, Germany, [17]Department of Chemistry and Molecular Biology, University of Gothenburg, Gothenburg, Sweden, [18]National Institute of Water and Atmospheric Research, Wellington, New Zealand, [19]Canadian Centre for Climate Modeling and Analysis, Environment Canada, Victoria, British Columbia, Canada, [20]Bodeker Scientific, Alexandra, New Zealand, [21]ETH Zürich, Institute for Atmospheric and Climate Science, Zürich, Switzerland, [22]Physikalisch-Meteorologisches Observatorium Davos World Radiation Centre, Davos Dorf, Davos, Switzerland, [23]Nagoya University, Graduate School of Environmental Studies, Nagoya, Japan, [24]Japan Marine-Earth Science and Technology, Yokohama, Japan

Abstract Formaldehyde (HCHO) directly affects the atmospheric oxidative capacity through its effects on HO_x. In remote marine environments, such as the tropical western Pacific (TWP), it is particularly important to understand the processes controlling the abundance of HCHO because model output from these regions is used to correct satellite retrievals of HCHO. Here we have used observations from the Convective Transport of Active Species in the Tropics (CONTRAST) field campaign, conducted during January and February 2014, to evaluate our understanding of the processes controlling the distribution of HCHO in the TWP as well as its representation in chemical transport/climate models. Observed HCHO mixing ratios varied from ~500 parts per trillion by volume (pptv) near the surface to ~75 pptv in the upper troposphere. Recent convective transport of near surface HCHO and its precursors, acetaldehyde and possibly methyl hydroperoxide, increased upper tropospheric HCHO mixing ratios by ~33% (22 pptv); this air contained roughly 60% less NO than more aged air. Output from the CAM-Chem chemistry transport model (2014 meteorology) as well as nine chemistry climate models from the Chemistry-Climate Model Initiative (free-running meteorology) are found to uniformly underestimate HCHO columns derived from in situ observations by between 4 and 50%. This underestimate of HCHO likely results from a near factor of two underestimate of NO in most models, which strongly suggests errors in NO_x emissions inventories and/or in the model chemical mechanisms. Likewise, the lack of oceanic acetaldehyde emissions and potential errors in the model acetaldehyde chemistry lead to additional underestimates in modeled HCHO of up to 75 pptv (~15%) in the lower troposphere.

1. Introduction

Formaldehyde (HCHO) is a pervasive trace gas that provides insight into the dynamical and chemical processes controlling atmospheric composition. The photolysis and subsequent photochemistry of HCHO is an important source of the hydroperoxyl radical (HO_2) in both urban (Volkamer et al., 2010) and remote (Mahajan et al., 2010; Whalley et al., 2010) regions. In the upper troposphere (UT), HCHO is a precursor of the hydroxyl radical (OH) (Jaegle et al., 1998), affecting the oxidative capacity of the atmosphere. Knowledge of the distribution of HCHO thus aids in constraining production of HO_x ($HO_x = OH + HO_2$) in chemical models. Because of its relatively short atmospheric lifetime, with a noontime minimum of ~2 h in the tropics, and its vertical concentration profile with surface values almost an order of magnitude larger than those in the UT, HCHO is also a suitable tracer for recent convection (e.g., Borbon et al., 2012; Fried et al., 2016, 2008). To understand the atmospheric HO_x budget, the chemistry and dynamical processes controlling HCHO must be thoroughly characterized.

The global atmospheric budget of HCHO is dominated by in situ production, with methane oxidation providing ~970 Tg yr^{-1} and oxidation of other hydrocarbons contributing an additional 250 Tg yr^{-1} (Fortems-Cheiney et al., 2012). There are minor primary emissions, on the order of 10 Tg yr^{-1}, from biomass burning (Akagi et al., 2011; Andreae & Merlet, 2001; Holzinger et al., 1999), industry (Friedfeld et al., 2002; Garcia et al., 2006; Parrish et al., 2012), agriculture (Kaiser et al., 2015), automobiles (Grosjean et al., 2001; Lipari & Swarin, 1982), shipping (Marbach et al., 2009), and vegetation (DiGangi et al., 2011). The short atmospheric lifetime of HCHO prevents long-range transport of these primary emissions to remote regions (Vigouroux et al., 2009). Oceanic emission has also been suggested as a primary source of HCHO in the remote marine environment (Zhou & Mopper, 1997). While isoprene and other volatile organic compounds (VOCs) are significant HCHO precursors in areas with large biogenic or anthropogenic emissions (Millet et al., 2006; Palmer et al., 2003; Wolfe, Kaiser, et al., 2016), in the remote marine environment, atmospheric HCHO is mainly produced by methane oxidation (Ayers et al., 1997), with minor contributions from acetone (Jaegle et al., 2000), methanol (Jaegle et al., 2000), acetaldehyde (Singh et al., 2004), and glyoxal (Coburn et al., 2014; Volkamer et al., 2015). This in situ production in remote regions typically results in HCHO mixing ratios from 200 to 400 parts per trillion by volume (pptv) near the surface and significantly lower values, frequently below 100 pptv, in the UT (Ayers et al., 1997; Fried et al., 2011, 2003; Frost et al., 2002; Heikes et al., 2001; Jones et al., 2009; Still et al., 2006). Unless otherwise indicated, HCHO production is used to indicate formation, not net HCHO production (i.e., formation minus loss).

Production of HCHO from methane is generally initiated by reaction with OH, $O(^1D)$, or Cl, producing the peroxymethyl radical (CH_3O_2). In a low NO_x regime, the peroxymethyl radical then reacts to form various species, including methyl hydroperoxide (MHP: CH_3OOH) and methanol (CH_3OH), before generating HCHO. Chemical sinks of HCHO include two photolytic pathways as well as reactions with OH, NO_3, Cl, and Br. Oxidation of HCHO by OH (R1) has no net effect on total HO_x, as HO_2 is converted to OH in the presence of sufficient NO_x. At low NO_x concentrations, however, oxidation of HCHO effectively partitions OH to HO_2, as the conversion of HO_2 to OH is inhibited (Gao et al., 2014). Photolysis is a significant source of H_2 (R2) and HO_2 (R3). Other removal mechanisms include dry and wet deposition (Economou & Mihalopoulos, 2002; Thompson, 1980; Tost et al., 2007) and processing in clouds (Amato et al., 2007; Barth, 2003; Tost et al., 2007). A schematic of the major reactions controlling HCHO abundance is shown in Figure 1.

(R1) $$OH + HCHO \rightarrow CO + H_2O + HO_2$$

(R2) $$HCHO + h\upsilon \rightarrow CO + H_2$$

(R3) $$HCHO + h\upsilon\ (+O_2) \rightarrow CO + 2HO_2.$$

Formaldehyde observations are limited in the tropical western Pacific (TWP). Peters et al. (2012), using differential optical absorption spectroscopy (DOAS), found total column HCHO to be between 2 and 4×10^{15} cm^{-2} in the TWP during October 2009 as part of the TransBrom cruise. These observations provided a diurnal profile of the HCHO column content but were limited to the narrow path of the ship track and provide no information about altitudinal variations of HCHO concentration. In situ aircraft observations of HCHO have often been limited by the low concentrations in the UT, frequently below the instrument detection limits (LODs). Heikes et al. (2001) measured HCHO with an enzyme derivatization fluorescence technique with a LOD of

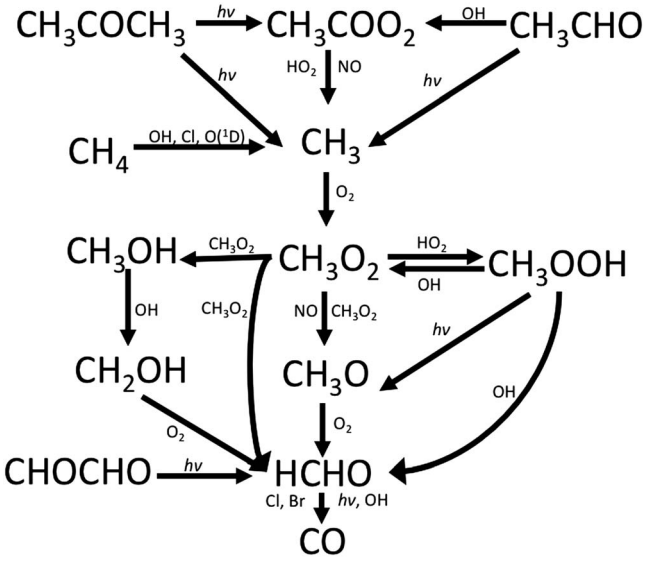

Figure 1. Schematic for the production of formaldehyde from acetone (CH_3COCH_3), acetaldehyde (CH_3CHO), methane (CH_4), methanol (CH_3OH), and glyoxal (CHOCHO). After Stickler et al. (2006).

50 pptv during the Pacific Exploratory Mission (PEM)-Tropics B campaign, conducted in the central Pacific during March to April 1999 at altitudes between the surface and ~12 km. More than 25% of observations were below the LOD, with median values at 8 km on the order of 100 pptv. Fried et al. (2003) measured HCHO with tunable diode laser absorption spectroscopy, with an LOD primarily between 50 and 80 pptv, in the western Pacific as part of the TRACE-P campaign (February to April 2001). Between 8 and 12 km, median HCHO values were 51 pptv in the western Pacific. While sampling the northern edge of the remote TWP, the TRACE-P campaign did not heavily sample the deep tropics or the tropical tropopause layer (TTL), located between about 14 and 18.5 km. The TTL acts as a transition zone between the tropical troposphere and stratosphere and is the site of significant deep convective outflow (Fueglistaler et al., 2009). Additional observations of HCHO in the deep tropics and UT in this region are therefore needed to complement these previous studies.

Agreement between observations of HCHO and model output varies dramatically among studies that focused on the remote, marine environment. Fried et al. (2011) showed that observations of HCHO over the eastern Pacific Ocean from the INTEX-B campaign (April to May 2006) could be reproduced by a photochemical box model from the surface to ~11 km and that methane was the dominant precursor. Jones et al. (2009) determined that methane chemistry alone is insufficient to produce HCHO comparable to surface observations in a remote New Zealand site as inferred from high-resolution Fourier transform infrared (FTIR) measurements. Vigouroux et al. (2009) compared column HCHO measured by FTIR and DOAS instruments at Réunion to output from the IMAGES global chemical transport model (CTM), finding that the model underestimated column HCHO by between 15 and 29%. These results, however, could have been affected by errors in the HCHO line parameters used in the retrieval, potentially biasing the HCHO retrieval high (e.g., Franco et al., 2015). Finally, Zeng et al. (2015) showed that four global chemistry models underestimated column HCHO by approximately 50% in the Southern Hemisphere, as compared to FTIR observations, suggesting that these models lack a significant source of HCHO. It is imperative to evaluate the vertical columns of these CTMs, particularly in remote locations, as many satellite retrievals use output from these models to correct for biases in the retrieval (e.g., De Smedt et al., 2015; González Abad et al., 2015, 2016; Li et al., 2015).

Here we use in situ observations of HCHO collected during the Convective Transport of Active Species in the Tropics (CONTRAST) campaign to characterize, for the first time, the distribution of HCHO in the TWP from the surface to approximately 15 km, the level of deep convective outflow. Back trajectories and satellite observations are used in conjunction with the in situ observations to determine the effects of convection on the HCHO mixing ratio. We then use observations of a suite of VOCs and other species from CONTRAST and a photochemical box model to evaluate our current understanding of HCHO chemistry and the oxidative capacity of the atmosphere. Finally, these observations are also compared to output from the CAM-Chem CTM and a suite of models from the Chemistry Climate Model Initiative (CCMI) to assess the representation of HCHO in global chemistry models.

2. Methodology

2.1. Campaign Description

The CONTRAST campaign consisted of 16 research flights conducted using the National Center for Atmospheric Research (NCAR) Gulfstream V (GV) aircraft during January and February 2014. For a complete description of CONTRAST, see Pan et al. (2016). Research flights (RF) were either based out of Guam (13.5°N, 144.8°E) or conducted in transit between Broomfield, CO (39.95°N, 105.1°W), and Guam. Flights from Guam spanned latitudes from the northern coast of Australia to Japan and altitudes from approximately 0.1 to 15 km. Vertical profiles of the tropospheric column were obtained on multiple flights, with most profiles spanning the full altitude range of the mission. While some profiles were obtained as spirals, most were ascents or descents made in a straight line and covering several hundred kilometers in the horizontal. Here data from

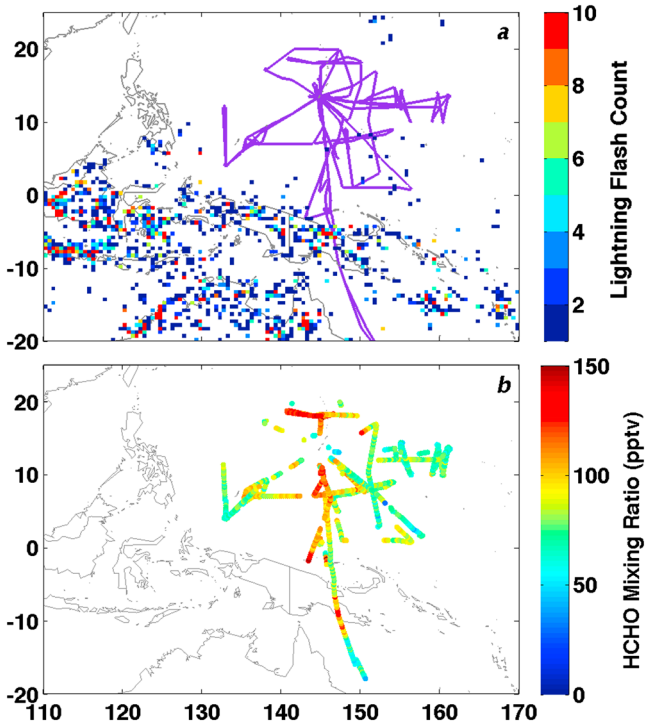

Figure 2. (a) Sum of lightning flash counts for January and February 2014 from the lightning imaging sensor on board the TRMM satellite (Cecil et al., 2014). Latitude and longitude for each lightning flash along the satellite track were downloaded from https://ghrc.nsstc.nasa.gov/hydro/. Data from each flight day and preceding day were sorted into a 0.5° × 0.5° horizontal grid and summed over the entire campaign. The CONTRAST flight tracks for all flights analyzed in this study are shown in purple. (b) Observed HCHO from ISAF at pressures less than 300 hPa. Data are averaged over the TOGA observation time and are limited to latitudes between 20°S and 20°N.

the transit flights (RF01, 02, and 16) and RF03, which lacked CO measurements, are excluded. Flight tracks analyzed here are shown in Figure 2a.

2.1.1. Formaldehyde Measurements

Formaldehyde was measured by the In Situ Airborne Formaldehyde (ISAF) instrument. A complete instrument description can be found in Cazorla et al. (2015), and only a brief summary is given here. ISAF relies on the laser-induced fluorescence technique. A pulsed UV fiber laser is tuned to a HCHO rovibronic absorption line at 353.163 nm. A fraction of the excited HCHO molecules relaxes to the ground state by fluorescence, and the resultant photons are counted by a photomultiplier tube. Nonresonant background signal is measured at a nearby wavelength (353.168 nm) with no HCHO absorption. The difference between the measurements at these two wavelengths is proportional to the mixing ratio of HCHO.

The instrument was calibrated before and after the campaign through standard dilution of a ~500 ppbv primary HCHO standard (Scott specialty gas) to zero air. The calibration factor is dependent on cell pressure, which affects the number density, absorption line broadening, and quenching of the sample. The concentration of the standard was determined through both long-path UV absorption and FTIR. FTIR measurements were corrected to the UV-determined value to tie the calibration to a literature standard, as described in Cazorla et al. (2015). Instrument performance is reliable over time, with the calibration factor varying by less than 10% between the two calibrations. Data are sampled by ISAF at 10 Hz and reported at 1 Hz. At 1 Hz, the 2σ LOD is 36 pptv, and the instrument precision is better than 20% above 100 pptv. For the upper tropospheric background observed in CONTRAST (between 50 and 75 pptv), instrument precision is closer to 30%, as uncertainty at these mixing ratios is dictated by variability in the nonresonant background signal. Overall measurement accuracy (1σ) is 10% + 20 pptv.

ISAF has been deployed on multiple field campaigns and been compared to observations from a difference frequency generation absorption spectrometer (DFGAS) (Weibring et al., 2006, 2007) during the DC3 campaign and a similar instrument during the SEAC^{4}RS campaign. For data from DC3, a regression of observations from the two instruments showed high correlation ($r^2 = 0.98$) with a slope and intercept of 0.86 and 63.4 pptv, with the ISAF observations higher than the DFGAS measurements by ~50 pptv (*G* Chen, 2017). Because of the low HCHO abundance in the UT, this difference was particularly notable at low pressures. Similar results were found for the SEAC^{4}RS campaign. The source of this disagreement is currently unknown, but the difference suggests a possible bias in one or both instruments.

Possible sources of a high bias in the ISAF measurement are in situ production of HCHO in the inlet, adsorption/desorption of HCHO on the inlet tubing, and possible contamination due to the inlet design. As discussed in section 3.3.1, measurement artifacts from the decomposition of methylperoxynitrate ($CH_3O_2NO_2$: MPN) and reactions of VOCs with ozone were likely negligible (<5 pptv). The large volumetric flow rate through the inlet, ~25 L min^{-1}, is designed to prevent any significant adsorption and later desorption of HCHO on the inlet tubing. Significant desorption of HCHO from the inlet tubing would result in higher mixing ratios at lower flow rates. There is no discernable relationship between observed HCHO mixing ratio and flow rate, with HCHO distributions at the same pressure but different flow rates being nearly identical (Figure S1 in the supporting information). While desorption cannot be completely excluded, this lack of variation of HCHO with flow rate suggests that the quantities desorbed are small. This is further supported by observation of HCHO on the order of 25 to 30 pptv at the lowest pressures (Figure S1). Because, as discussed in section 3.3.2, methane is the dominant HCHO precursor and it is ubiquitous in the atmosphere, a background of at least 10 to 15 pptv HCHO would be expected even in the tropical UT. This would suggest that desorption could be a source of measurement interference of no more than 20 pptv of HCHO, on the order of the measurement uncertainty.

Finally, after the campaign, it was discovered that a portion of the inlet Teflon tubing had melted at an unknown time during CONTRAST. The inlet design, however, makes it unlikely that the HCHO observations were contaminated by the melted Teflon. A schematic of the inlet is shown in Figure S2. The inlet was mounted on the top of the plane with a portion of the air flow subsampled perpendicular to the flight direction. This section of the inlet (portion A in Figure S2) had been catheterized with stainless steel tubing that was sealed from the Teflon tubing via an air-tight O-ring. Because the melted Teflon was downstream of the stainless steel inlet and O-ring seal, contamination from cabin air and/or other air in the inlet is unlikely. In addition, there was no significant difference in observed HCHO profiles over the course of the campaign, suggesting that the melted Teflon did not influence the measurements.

2.1.2. Additional Trace Gas Observations

The NCAR GV aircraft was outfitted to measure various trace gases, meteorological parameters, and radiative flux. Ozone and NO were measured by chemiluminescence (Ridley & Grahek, 1990). Total 2σ uncertainties, averaged over 35 s, were 1.2 ppbv and 4.5 pptv for O_3 and NO, respectively. Ozone and NO have been corrected for quenching due to ambient water vapor (Ridley et al., 1994). Carbon monoxide was also measured at 1 Hz, with an Aerolaser 5002 vacuum ultraviolet fluorescence instrument (Gerbig et al., 1999) with a 2σ uncertainty of 3 ppbv ± 3%. Methane was measured by wavelength-scanned cavity ringdown spectroscopy using a Picarro G1301-c analyzer (Crosson, 2008). Measurement uncertainty is 3 ppbv (2σ) for a 0.2 s averaging time. Water vapor was measured by an open-path, laser hygrometer (Zondlo et al., 2010). Data were reported at 1 Hz with a 2σ precision of $<$3%. Photolysis frequencies were calculated from actinic flux density by the High-performance Instrumented Airborne Platform for Environmental Research (HIAPER) Airborne Radiation Package (HARP) on board the GV aircraft during CONTRAST (Petropavlovskikh et al., 2007). Estimated total, 1σ uncertainties in photolysis frequencies relevant to this study are ±25%, ±12%, and ±20% for j_{O1D}, j_{NO2}, and both HCHO photolysis pathways, respectively.

The Trace Organic Gas Analyzer (TOGA) instrument measured a suite of trace gases via gas chromatography/quadrupole mass spectrometry (GCMS) with a sampling time of 35 s and 2 min between sampling periods (Apel et al., 2010). Unless otherwise indicated, all data in this study have been averaged over the TOGA sampling period so that all observations have the same time coordinate. Measured species relevant to this study are acetone, acetaldehyde, propanal, butanal, benzene, methanol, acrolein, propane, *n*-butane, *i*-butane, *n*-pentane, *i*-pentane, isoprene, and the isoprene decomposition products methyl vinyl ketone and methacrolein. Measurement uncertainties and LODs for these species are listed in the supporting information Table S1. Additional trace gas measurements were made by the Advanced Whole Air Sampler (AWAS) instrument. AWAS acquires up to 60 samples of ambient air per flight in electropolished stainless steel canisters. Sampling time is pressure dependent, with times ranging between about 10 and 60 s. Canisters were analyzed postflight using GCMS. AWAS measurements used in this study are ethane, *n*-butane, *i*-butane, *n*-pentane, *i*-pentane, ethyne, and benzene.

BrO was measured remotely with the Airborne Multi-Axis (AMAX) DOAS instrument (Baidar et al., 2013; Volkamer et al., 2015) and in situ via chemical ionization mass spectrometry (CIMS) (*D* Chen et al., 2016; Liao et al., 2012). The BrO LOD for a 60 s sampling time is ~0.3 pptv for AMAX DOAS. In addition to BrO, the CIMS instrument measured HOBr and Br_2. These two species were reported as their sum, however, because of possible conversion of HOBr to Br_2 in the sample inlet. Detection limits for BrO and HOBr + Br_2 were 0.6 to 1.6 pptv and 1.3 to 3.5 pptv, respectively.

In addition to the measurements from the CONTRAST CIMS instrument, observations of inorganic halogens from a CIMS instrument in the Coordinated Airborne Studies in the Tropics (CAST) campaign are also used (Harris et al., 2016). CAST, also based out of Guam, was conducted simultaneously with CONTRAST and made observations in the lower troposphere, primarily from 30 m above mean sea level to approximately 8 km. A CIMS instrument with similar operating parameters as that used in CONTRAST measured, among other species, BrO, Br_2, HOBr, and HCl (Le Breton et al., 2017).

2.2. Box Model Setup

Formaldehyde mixing ratios were modeled with the Framework for 0-D Atmospheric Modeling version 3.1 box model (Wolfe, Marvin et al., 2016). The model was run with a subset of the Master Chemical Mechanism (MCM) (Jenkin et al., 2003; Saunders et al., 2003) version 3.3.1 (Jenkin et al., 2015). Inorganic bromine and chlorine chemistry from the Module Efficiently Calculating the Chemistry of the Atmosphere v 3.0

(Sander et al., 2011) and the reaction of methane with O^1D (Atkinson et al., 2006) were also included. The model was run forward in time with a model time step of 1 h, with all constrained concentrations and meteorology held constant but photolysis frequencies varying with time of day. The diurnal cycle was repeated for 4 days for each set of observations, which was found sufficient to bring HCHO into steady state.

The model was constrained with observations taken during CONTRAST of temperature, pressure, relative humidity, O_3, NO, CO, CH_4, methanol, acetone, acetaldehyde, propanal, butanal, acrolein, isoprene, methanol, propane, ethyne, and benzene. Observational constraints were averaged over the TOGA sampling interval, and only intervals with simultaneous observations of CO, O_3, NO, CH_4, relative humidity, and HCHO were used. The modeled intervals were further restricted to aircraft sampling between 20°S and 20°N at a solar zenith angle (SZA) less than 60°. Missing data for other species were linearly interpolated in time. Because of the high frequency of observations by the TOGA instrument below the LOD in the UT, we estimate any TOGA observations below the detection limit at 30% of the LOD. Including the linearly interpolated data and the data points with TOGA observations below the LOD increases the number of data points available for modeling from 342 to 612, providing more robust statistics. As discussed in section 3.3.1, including these data points does not affect our results. The model was also constrained to estimates of ethene as described below and to various halogen species (BrO, HOBr, Cl, Br_2, and Br) as described in the supporting information Texts S1–S2.

Ethyne, which was measured only by the AWAS instrument and at a sampling frequency less than that of the TOGA species, was linearly interpolated to the TOGA observation time. For times before and after AWAS observations began as well as for flights without AWAS observations, ethyne mixing ratios were estimated from the median, campaign-wide vertical profile. Ethene mixing ratios were not measured during CONTRAST and are taken from the CAM-Chem model, described below. The ethene profile from CAM-Chem (Figure S3) is comparable to that from previous field campaigns (Blake, 2003). When the box model was run with double these ethene concentrations, modeled HCHO varied by 1–2%, on average.

Photolysis rates are allowed to vary with the diel cycle, and as such, parameterizations are used to calculate the photolysis frequency at SZAs other than that at the observed time. To calculate the photolysis frequency for a given species, we use reaction dependent parameterizations provided by the MCM, described by equation (1). Here χ is SZA and l, m, and n are species-specific coefficients. These modeled photolysis rates are then multiplied by a scaling factor determined by calculating the ratio of the HARP observations to modeled photolysis frequencies at the time of observation to take into account, as best as possible, variations in albedo and overhead column O_3 not considered in the MCM parameterization. For photolysis reactions of halogen species, which are not included in the MCM, the terms l, m, and n for equation (1) were determined for each halogen species by fitting SZA-binned observations of photolysis frequencies from all flights conducted in the tropics to equation (1) as described in Jenkin et al. (1997). Photolysis frequencies were then calculated and scaled as for the other reactions.

$$j = l(\cos\chi)^m \exp(-n \times \sec\chi) \quad (1)$$

2.3. Convective Influence

To determine whether an air parcel had been convectively lofted, a combination of back trajectories and satellite data were used. Ten day kinematic back trajectories along the flight track were calculated using the NOAA Hybrid Single-Particle Lagrangian Integrated Trajectory model (Stein et al., 2015). The trajectories allowed for vertical displacement, using estimates of the vertical wind from assimilated meteorological fields. Trajectories were initialized at each observation time corresponding with the TOGA instrument for all flights analyzed here. Global Data Assimilation System meteorological fields at 1° latitude × 1° longitude drove the model.

To estimate when an air parcel was last convectively lofted, we combine these back trajectories with satellite observations of precipitating convection, as discussed in Anderson et al. (2016), in which this approach was used to determine the origin of high ozone low water structures in the TWP. Precipitation rates from the Tropical Rainfall Measuring Mission (TRMM) multisatellite precipitation analysis product (Huffman et al., 2007) were combined with cloud top heights calculated from geostationary satellite infrared measurements to determine the location of convection as described in Bergman et al. (2012). The convective precipitation product is available at 0.25° latitude × 0.25° longitude resolution with a time step of 3 h. Intersection of a trajectory with precipitating convection was defined as a point on the trajectory being within 25 km of convection in the horizontal and being at or below the cloud top height. While any given trajectory likely has a large

uncertainty that increases with distance from the initiation point, the number of trajectories used in this analysis (~400 for air parcels experiencing convection within 24 h of observation) acts to reduce this uncertainty. As a result, as discussed in section 3.2, our results are relatively insensitive to this interception radius for radii up to at least 100 km. In addition, because the satellite product only captures precipitating convection, it is possible that this method fails to capture air parcels that have been convectively lofted in nonprecipitating events.

2.4. Chemistry Transport and Chemistry Climate Models

2.4.1. CAM-Chem

The Community Atmosphere Model version 4.0 (CAM4) is the atmospheric component of the global chemistry-climate model Community Earth System Model (CESM) (Lamarque et al., 2012). When run with active chemistry, it is known as CAM-Chem. Here the model was run off-line, with meteorological fields specified by the NASA GEOS5 model (Tilmes et al., 2015), with a horizontal resolution of 0.94° latitude × 1.25° longitude and 56 vertical levels. The model chemistry scheme includes a detailed representation of tropospheric and stratospheric chemistry (~180 species and ~500 chemical reactions), including very short lived halogens. Fernandez et al. (2014) provide details on surface emissions, wet and dry deposition, heterogeneous reactions, and photochemical processes of halogens used within CAM-Chem. Anthropogenic emissions are from the Representative Concentration Pathway (RCP) 6.0 scenario (Meinshausen et al., 2011; van Vuuren et al., 2011), and biomass burning emissions are from the Fire Inventory for NCAR (FINN) (Wiedinmyer et al., 2011).

2.4.2. CCMI

CCMI is a model intercomparison project in which approximately 24 chemistry climate models (CCMs) are run with the same set of anthropogenic emissions and climate forcers. See Morgenstern et al. (2017) for a complete listing of the emissions inventories and climate forcers used as well as a high-level description of the CCMI models. Model output has been archived by the CCMI project and maintained at the British Atmospheric Data Centre (BADC, http://badc.nerc.ac.uk/, last accessed July 2017). Among the goals of CCMI are understanding trends in tropospheric ozone and understanding the controlling mechanisms for OH. Here we evaluate only the nine CCMs that archived monthly output of both HCHO and NO, a species instrumental in HCHO production: CESM1-WACCM (Tilmes et al., 2016), CHASER (MIROC-ESM) (Watanabe et al., 2011), CMAM (Scinocca et al., 2008), GEOSCCM (Oman et al., 2013), MOCAGE (Guth et al., 2016; Josse et al., 2004), NIWA-UKCA (Morgenstern et al., 2013), SOCOL3 (Stenke et al., 2013), and two setups of EMAC (Jöckel et al., 2010, 2016). Chemical mechanisms vary widely among the models. CMAM does not consider the chemistry of nonmethane hydrocarbons (NMHCs), while the only NMHC source gas considered by SOCOL3 is isoprene. The other models include a more expansive suite of NMHCs.

All model output, except for that from CHASER, is from the REF-C1 hindcast scenario, in which the models simulate the atmosphere from 1960 to 2010 with free-running meteorology but are constrained to prescribed sea surface temperatures and sea ice. CHASER output is, at the time of writing, only available for the REF-C1SD scenario, which uses the same emissions and forcers as the REF-C1 scenario but is constrained to a specified meteorology. As discussed in section 3.4.2, we use the hindcast scenario, and not the forecast scenario (REF-C2), which includes 2014, because more model output is available for the REF-C1 scenario and models show little interannual variability in either NO or HCHO during the years examined here (2001–2010).

3. Results and Discussion

3.1. Formaldehyde Distribution

The vertical profile of all HCHO observations made in the TWP is shown in Figure 3. Near-surface values (observations between the surface and 975 hPa) had a median mixing ratio of 506 pptv (Figure 3). Formaldehyde was highest near Papua New Guinea, where isoprene and direct emission of HCHO from biomass burning likely increase HCHO as compared to the TWP background. Formaldehyde mixing ratios decay exponentially with decreasing pressure, reaching a median value of 74 pptv in the UT at pressures less than 300 hPa. Local, upper tropospheric maxima of HCHO, with values exceeding 140 pptv, were found north of Guam and near Papua New Guinea (Figure 2b). The maximum north of Guam was observed during a flight designed to measure fresh, convective outflow, suggesting that convective transport of near-surface air,

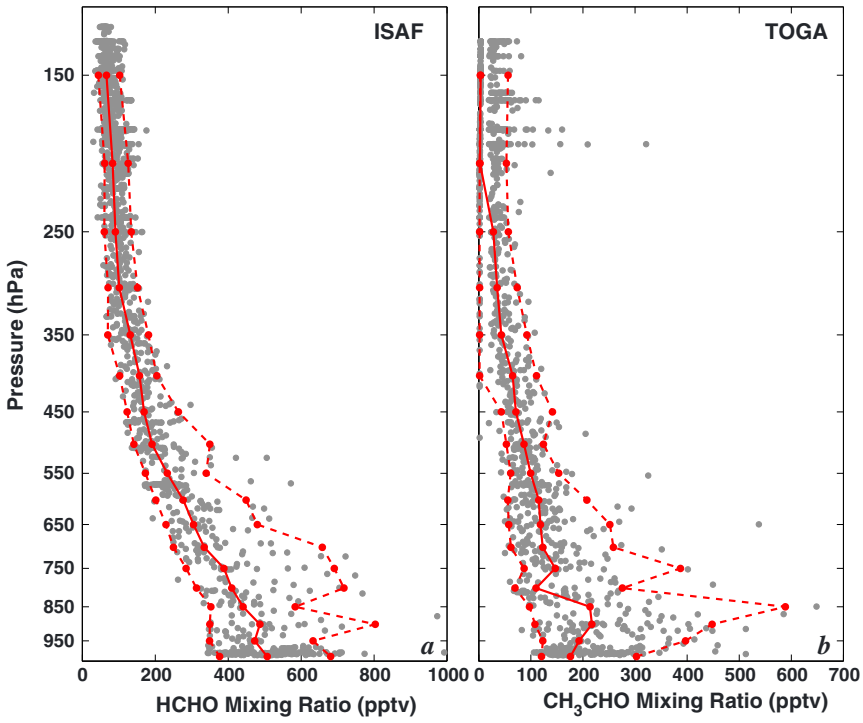

Figure 3. Measured (a) formaldehyde (HCHO) from ISAF averaged over the TOGA sampling interval and (b) acetaldehyde (CH_3CHO) from TOGA (gray). The 5th, 50th, and 95th percentiles for 50 hPa pressure bins are shown in red.

rich in HCHO and its precursors, is a likely cause for these high upper tropospheric values. Convective influence on the distribution of HCHO is explored more fully in section 3.2. Vertical profiles and the upper tropospheric distribution of HCHO from flights not analyzed in depth in this paper (RF 01–03 and 16) are shown in Figure S4. In general, upper tropospheric HCHO was slightly lower during these research flights, driven by values on the order of 40–50 pptv measured between Hawaii and Guam. We do not analyze these flights in more detail, however, because of the low frequency of sampling in these regions.

CONTRAST measurements of HCHO between 8 and 12 km were almost a factor of 2 higher than that observed during TRACE-P, with medians of 97 and 51 pptv, respectively. This increased HCHO could result from differences in spatiotemporal sampling as well as the phase of the El Niño–Southern Oscillation (ENSO). Most TRACE-P observations were made north of the CONTRAST domain and in March through April, while CONTRAST took place in January and February. In addition, during TRACE-P, ENSO was in a weak La Niña phase, shifting convection westward (Fuelberg, 2003), as compared to during CONTRAST, which was conducted during a weak El Niño. This shift in convection would result in less transport of HCHO and its precursors into the UT during TRACE-P. In addition, there is an offset between ISAF and the infrared absorption technique used in TRACE-P, suggesting that instrumental differences could also account for the change in HCHO values between the two campaigns.

Total tropospheric column HCHO was calculated for each profile with observations throughout the troposphere. See the supporting information for a description of the column calculation technique. The tropospheric formaldehyde column ranged from 4.1 to 7.5 $\times$ 10^{15} cm^{-2}, with a mean value of 5.6 $\pm$ 0.86 $\times$ 10^{15} cm^{-2} (1σ). While it is possible that horizontal heterogeneities may affect the calculation of the HCHO columns, in general, as shown in Figure 3, there was little variation in HCHO mixing ratios at a given pressure level. Three complete HCHO columns were obtained during RF06, in which the aircraft sampled air masses on either side of a frontal system west of Guam. Air behind the front had consistently higher mixing ratios of anthropogenic pollutants, while air ahead of the front was more representative of pristine, marine air. Despite this difference in composition, there was only a 6% increase in column HCHO content behind the front (5.5 $\times$ 10^{15} cm^{-2}) compared to ahead of the front (5.2 $\times$ 10^{15} cm^{-2}). This difference is well within the variability of the observed columns in the tropics, suggesting that photochemical HCHO

production in aged, anthropogenically influenced air masses is not sufficient to perturb the tropical background tropospheric HCHO column significantly.

3.2. Convection, Aldehydes, and Upper Tropospheric HO_x

Convection and convective lofting of near surface species alters the chemical composition of the UT. Recent convection shifted the distribution of HCHO in the UT upward, increasing the median by 33% (22 pptv) from the aged air to air that had been convected within 24 h of observation (Figure 4). Here we define aged air as that which has not been convectively perturbed within 100 h before observation. This definition of aged air is consistent with the average time needed to advect air from Southeast Asia (5 ± 4 days) and allows for the dissipation of any convective effects. In addition, the radius used to determine the intersection of a back trajectory with convective precipitation has little effect on the results. (See section 2.3 for a description of the convection product.) Figure S5 shows the same information as Figure 4 but assuming a 100 km radius of interception. The change in HCHO between the convective and aged case, as well as the change for the other species shown, is nearly identical when increasing the interception radius from 25 to 100 km.

The distribution of chemical tracers in the UT is also consistent with our method of determining time since an air parcel encountered convection. Dimethyl sulfide is emitted from the ocean and has a lifetime on the order of hours (e.g., Barnes et al., 2006), resulting in a vertical profile that decays exponentially with height (Figure S6). During CONTRAST, only 12 observations above the LOD were made at pressures less than 300 hPa for the flights considered here. Consistent with its short lifetime, our method of determining time since convection classifies 11 of these air parcels as having been convected within 24 h of observation. Methyl iodide (CH3I), another short-lived marine air tracer (e.g., Ravetta et al., 2001), has a lifetime of ~4 days (Bell et al., 2002). The ratio of the median CH3I in recently convected air to aged air is 1.24 (Figure S7). Because our definition of aged air (100 h) is still within one lifetime of CH3I, some convective signature might still be apparent in air we classify as aged. When we increase our definition of aged air to 150 h, the ratio of CH3I in convected to aged air increases to ~1.75, consistent with Ravetta et al. (2001). While there is substantial overlap between the distributions for the aged and recently convected air, the near surface values (Figure S6) of CH_3I also showed significant variability, suggesting that there is no threshold mixing ratio of CH_3I in the UT that would indicate convection across the entire CONTRAST study region. Similar results are found for CH_3Br and $CHBr_3$ (Figures S6 and S7). Finally, the distributions of ozone and water vapor further support our determination of recently convected versus aged air. In the CONTRAST region, background marine air is characterized by low O_3 (~20 ppbv) and high relative humidity, while more aged air has the opposite signature (e.g., Anderson et al., 2016; Pan et al., 2016, 2015). Our analysis shows that the convectively controlled air has almost a factor of 2 lower ozone than the more aged air, while the water vapor mixing ratio is a factor of 3 higher in the recently convected air.

Because of the short atmospheric lifetime of HCHO in the UT, ~2 h, and the 33% higher HCHO in the recently convected air, convection must promote additional photochemical HCHO production in the UT through the transport of longer-lived HCHO precursors, such as acetaldehyde and MHP. Convection increases upper tropospheric acetaldehyde, a short-lived species with a vertical profile similar to that of HCHO (Figure 3b), from 2 pptv to 24 pptv (Figure 4). In situ production of acetaldehyde in the TWP UT is minimal; in the absence of deep convection, the upper tropospheric mixing ratio was frequently below the LOD. Box modeling analysis, discussed below, suggests that convectively influenced air parcels with the median mixing ratio of acetaldehyde (24 pptv) or higher, can provide between 10 and 20 pptv of additional HCHO over the background. The source of this acetaldehyde is uncertain, however. With an atmospheric lifetime on the order of 1 day, long-range transport of direct emissions from fires or biogenic sources is unlikely, suggesting a possible oceanic source (Millet et al., 2010) or significant in situ production (Read et al., 2012). Entrainment of acetaldehyde and its precursors from the midtroposphere, which contained emissions from biomass burning (Anderson et al., 2016), is a possible source of the higher CH_3CHO in the recently convected air (see, for example, Fried et al., 2016). Analysis of the biomass burning tracers HCN and CH_3CN shows conflicting results, however, with HCN lower in recently convected air and CH_3CN higher (Figure S7). Further investigation into the impacts of entrainment, though beyond the scope of this paper, is warranted.

As discussed in section 3.3.1, convective lofting of MHP and, to a lesser extent, glyoxal and ethene could also increase upper tropospheric HCHO in the convective case, although none of these species was measured during CONTRAST. Finally, calculated OH mixing ratios are 1.4 times lower in the freshly convected parcels

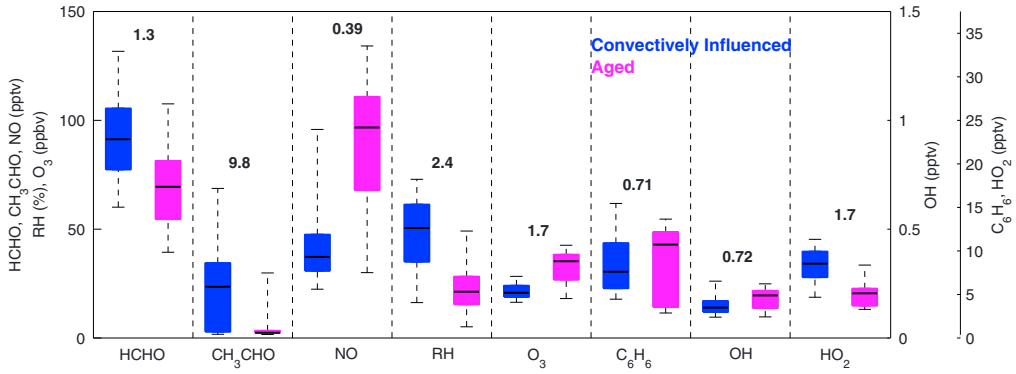

Figure 4. Distribution of observed trace gases for convectively influenced air parcels, defined as those that have been convectively lofted within 24 h of observation (blue), and aged air parcels, those that have not been convectively lofted within 100 h of observation (magenta). The 5th, 25th, 50th, 75th, and 95th percentiles are shown for observations between 150 and 300 hPa. The ratio of the medians of the convectively influenced to aged air parcels is also indicated for each species. OH and HO_2 are output from the F0AM box model from a run in which, in addition to the parameters used in the base case, the model was also constrained to HCHO observations. The low NO in convectively influenced air indicates the lack of lightning NO_x production in the TWP.

than in the aged air parcels (Figure 4), resulting in an increase in the lifetime of HCHO with respect to OH removal from ~24 to ~34 h. As discussed in section 3.3.2, in the UT, photolysis is responsible for ~90% of HCHO removal and the lifetime of HCHO with respect to photolysis during CONTRAST was ~2 h, suggesting that the lower OH values in the convectively lofted air likely have minimal influence on the higher HCHO in the convected air parcels.

Both HCHO and acetaldehyde are sources of HO_2, suggesting that increased upper tropospheric mixing ratios promoted by convection could lead to increased HO_2 production. Figure 5 shows the HO_2 production rates from photolysis of HCHO (squares) and acetaldehyde (diamonds) as calculated by the F0AM box model run constrained to HCHO observations. In the lower troposphere, there is no significant difference in HO_2 production between the convectively influenced and aged air parcels. At pressures less than 250 hPa, HO_2 production from HCHO and acetaldehyde is a factor of 2 and an order of magnitude larger, respectively, in the freshly convected air than in the aged air. Total HO_2 production from all sources is also shown in Figure 5 (circles) but does not show a significant difference between the convective and aged cases. Although convection significantly enhances the HO_2 production rate from acetaldehyde as compared to the aged case, the HO_2 production rate from acetaldehyde at 150 hPa is only 1.7% and 0.23% of the total HO_2 production rate for the convective and aged cases respectively. Thus, production of HO_2 from acetaldehyde photolysis is unimportant in the UT in either case. For HO_2 production from HCHO, however, the contribution to total HO_2 production increases from 7.5% to 11% from the aged to the convective case. Previous research in the TWP suggests that convective transport of MHP (Prather & Jacob, 1997) and H_2O_2 (Jaegle et al., 1997) from the MBL was the dominant factors in controlling tropical, upper tropospheric HO_x and that contributions from HCHO were insignificant. Production of HO_2 from HCHO photolysis is important during the CONTRAST campaign, although, as discussed below, MHP oxidation contributes to HCHO production in the UT.

The anthropogenic influence on the aged air alters the partitioning of HO_x compared to convectively influenced air parcels, driving HO_x from HO_2 to OH via reaction with NO. Calculated HO_2 is a factor of 1.7 higher in the convectively influenced air than in the aged air (Figure 4). Conversely, OH and NO are 1.4 and 2.6 times higher in the aged air than the tropically controlled parcels, respectively. OH is produced through photolysis of O_3 and the subsequent reaction of the $O(^1D)$ radical with H_2O as well as through the reaction of HO_2 with NO. The low NO mixing ratios in the pristine marine air lead to slow conversion of HO_2 to OH by (R4). Production of lightning NO_x in the convectively influenced air is apparently negligible, as demonstrated by the low NO mixing ratios and the low lightning flash count in the CONTRAST study region (Figure 2a). Even though the water vapor mixing ratio is 3 times higher in the convectively influenced case, the median value is still low in both cases because of the cold, upper tropospheric temperatures, resulting in slow primary production of OH.

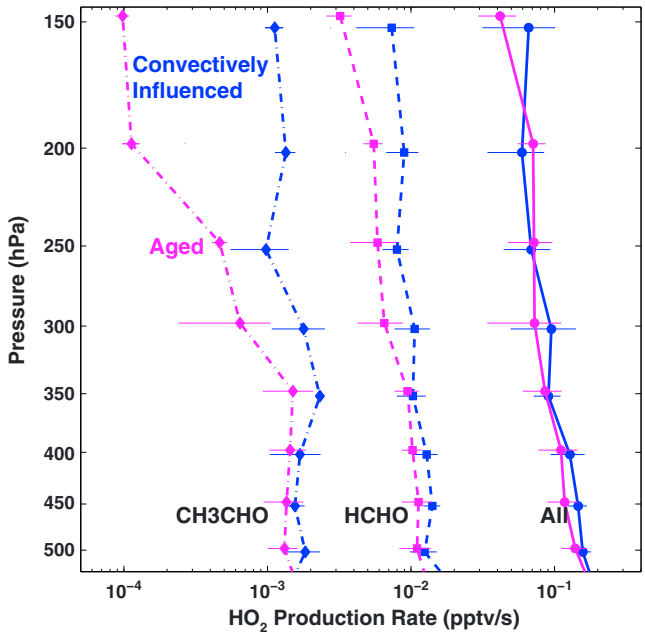

Figure 5. Production of HO_2 for aged (magenta) and convectively influenced (blue) air. The contribution from all species (circles and solid lines) as well as that from photolysis of formaldehyde (squares and dashed lines) and acetaldehyde (diamonds and dash-dotted lines) as output by the F0AM box model are shown. Modeled rates are from a run constrained by observations of HCHO, in addition to the constraints used in the baseline run. Convectively influenced air is defined as that which has been convectively lofted within 24 h of observation, while aged air has not been convectively lofted within 100 h.

(R4) $HO_2 + NO \rightarrow NO_2 + OH.$

Elevated benzene, with an atmospheric lifetime on the order of 6 days, suggests long-range transport of anthropogenic pollution in the aged air. Anderson et al. (2016) show that in the midtroposphere (300 to 700 hPa), the high abundances of NO observed during CONTRAST result from transport of biomass burning emissions with the possible influence of lightning generated NO_x from outside of the TWP. Here as discussed above, it is uncertain whether biomass burning has a strong influence on composition in the UT, making the source of this high NO unknown. NO from this pollutant source forces the equilibrium between the two HO_x species to higher OH and lower HO_2 than in the tropically influenced air. This is in contrast to the midtroposphere where the combination of high O_3 and low H_2O in the polluted air actually leads to lower OH as compared to the convectively controlled background (Nicely et al., 2016), and the high values of HCN clearly point to a biomass burning origin (Anderson et al., 2016).

3.3. Box Model Results

In the previous section, we investigated the distribution of HCHO and how it is affected by convection. We now transition to an evaluation of our understanding of how this HCHO distribution is controlled chemically, by using a photochemical box model. First, we evaluate the agreement between the model and observations, and then we use the model to determine the dominant species and processes controlling HCHO abundance. Using the results of the previous section, we also determine how convectively lofted species—like acetaldehyde, ethene, and MHP—affect HCHO production.

3.3.1. Box Model Evaluation

We use the F0AM box model driven by the MCM to evaluate our understanding of the chemistry, sources, and sinks driving the distribution of HCHO in the TWP. The box model generally captures mixing ratios of HCHO in the lower troposphere accurately. The results of the box modeling analysis (Figures 6 and 7) include only data points that had not experienced convection within the previous 24 h, to allow us to focus on air parcels for which HCHO production is likely under local photochemical control (i.e., production and loss have sufficient time to achieve a balance). The high r^2 (0.84) for a linear least squares regression between the box model output and the in situ observations (Figure 7a) suggests that the model is able to capture variations in HCHO mixing ratios. At pressures greater than 500 hPa, the observations and modeled HCHO agree within 10% (Figure 6c), indicating that the chemistry controlling HCHO abundance in the lower troposphere for the present marine environment is well characterized. The ratio of measured to modeled near-surface HCHO (pressures >900 hPa) is slightly less than unity (0.90). This overestimate of HCHO likely results from the lack of deposition in the model and also suggests that direct oceanic emissions are not an important source of HCHO in the TWP. While the model and observations agree on average, the accuracy of individual data points varies widely, with the absolute difference between measured and modeled HCHO ranging between −300 and 300 pptv. For pressures between 500 and 900 hPa (Figure 6a), the model slightly underestimates the HCHO mixing ratio, on average, but values lie within the 1σ spread of the observations. The number of observations in each pressure bin is shown in Figure 6c. These results are insensitive to the inclusion of modeled data points below the LOD and with interpolated data to fill data gaps, as shown in Figure S8. We therefore include all modeled data points to provide more robust statistics.

At pressures less than 500 hPa, the box model underestimates the observed mixing ratios by 50 to 60 pptv, suggesting inadequacies in the chemical mechanism for production of HCHO from known source gases, missing loss processes, missing HCHO precursors, or possible measurement artifacts. Modeled HCHO ranges from a mean of 130 pptv at 450 hPa to 19 pptv at 150 hPa, which translates to measured to modeled ratios of 1.40 and 3.96, respectively. While this ratio increases with decreasing pressure, the absolute difference

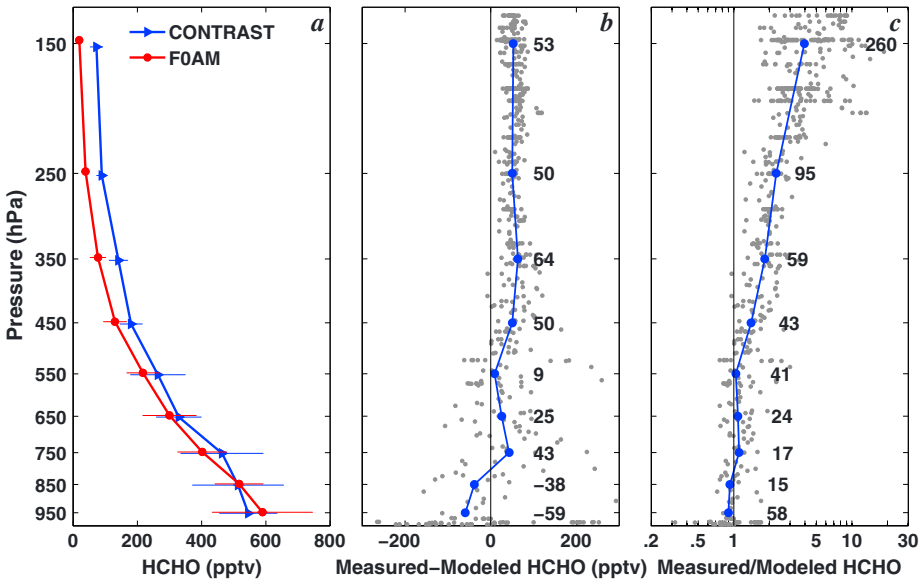

Figure 6. (a) Mean values of observed (blue) and F0AM modeled (red) formaldehyde in 100 hPa pressure bins for air parcels not being convectively lofted within 24 h of observation. Error bars are one standard deviation about the mean. (b) The difference between measured and modeled formaldehyde (gray). Mean values for 100 hPa pressure bins are shown in blue. Numbers indicate the average measured minus modeled difference. (c) Same as Figure 6b but the ratio of measured to modeled HCHO. Numbers indicate the number of observations/modeled points in each pressure bin.

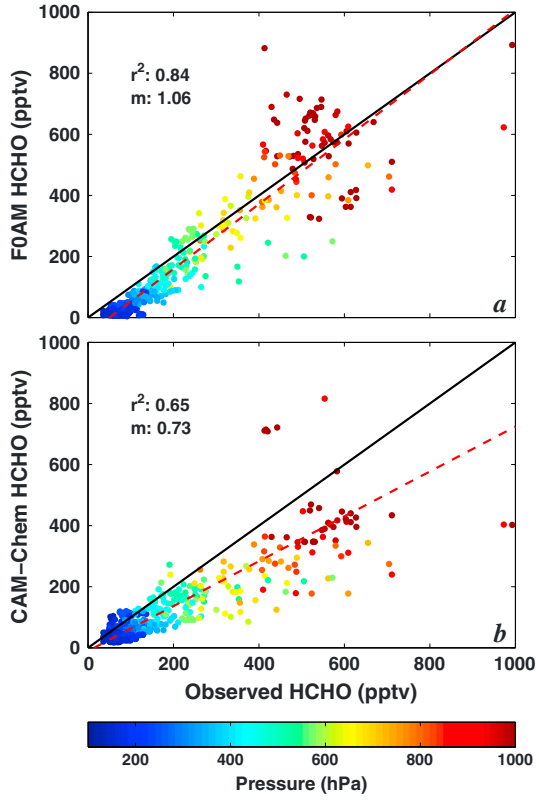

Figure 7. Regression of measured to modeled HCHO mixing ratios from (a) the F0AM box model and (b) CAM-Chem colored by pressure. F0AM output are from the base run, and CAM-Chem output was sampled along the flight track. The one-to-one lines are shown in black, and the lines of best fit, found using a linear least squares regression, in red. The slope (m) and r^2 are also shown.

between the measured and modeled HCHO stays relatively constant, ranging between 50 and 64 pptv (Figure 6b). This low bias in the model is in disagreement with the results found in Fried et al. (2003), who compared box modeled HCHO over the Pacific to observations from TRACE-P. While results in the lower troposphere from TRACE-P are similar to that found here, they found no systematic bias in box modeled HCHO in the region, with differences between measurement and model generally remaining within about 37 pptv.

Observational uncertainties could contribute to the difference between the measured and modeled values. Multiple box model runs were conducted in which observations of a given species were perturbed by its 2σ measurement uncertainty in both the positive and negative direction for RF11. Total uncertainty for NO and O_3 were calculated for each modeled data point. Although it is too computationally expensive to perform this analysis for all modeled data, the results for RF11 can be considered representative of the entire campaign. Figure 8 shows the percentage change in HCHO from the base model run caused by these perturbations for all species used to constrain the box model calculations, as well as total uncertainty, found by adding the individual uncertainties in quadrature. In the lower troposphere, where there is relatively good agreement between observations and the model, the total uncertainty (2σ) in modeled HCHO due to the measurement uncertainty is 21% (Figure 8b). The dominant contributors to this uncertainty are NO (7%), Cl (8%), $j_{HCHO(HCO)}$ (8%), j_{NO2} (9%), and $j_{HCHO(H2)}$ (13%), where HCHO(HCO) and HCHO(H_2) refer to the HCHO photolysis pathways in reactions (R3) and (R2), respectively. This low uncertainty shows significant improvement over earlier campaigns in remote regions, where instrument uncertainties were often a limiting factor in understanding HCHO chemistry (Wagner et al., 2002). In the UT, total uncertainty in

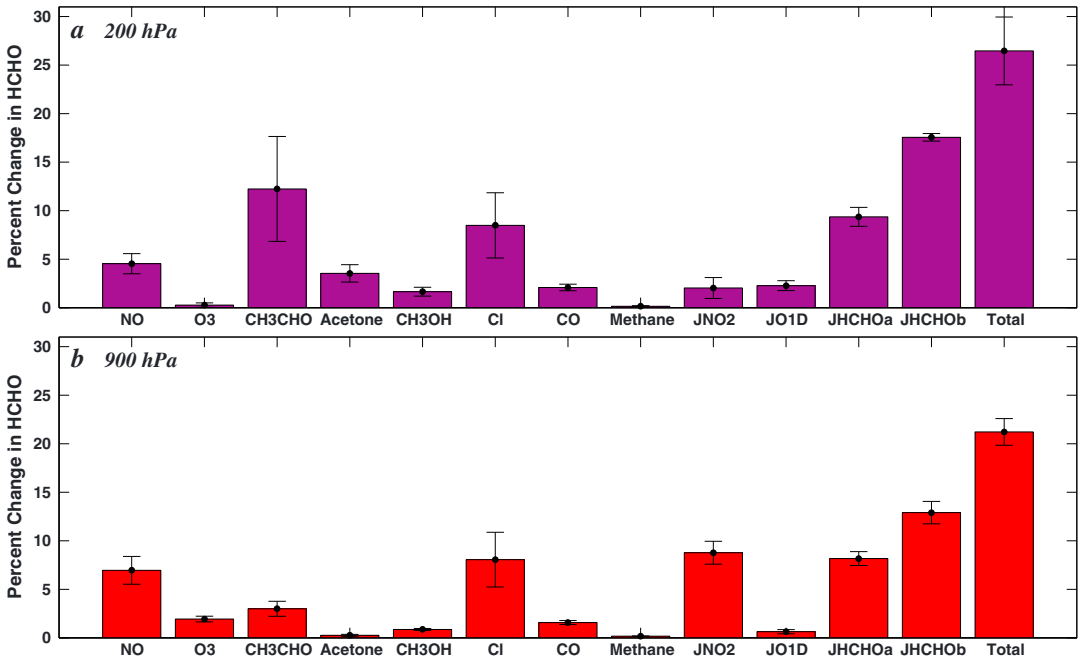

Figure 8. The percent uncertainty in the F0AM modeled HCHO value for RF11 (13 February 2014) for pressures between (a) 150 and 250 hPa and (b) 850 and 950 hPa. Each value is the mean of the absolute value of the percent change in HCHO found by perturbing the indicated observed species by the 2σ uncertainty of the measurement in both the positive and negative directions. Error bars show one standard deviation of the mean uncertainty. Total uncertainty is found by adding the uncertainty associated with each species in quadrature. JHCHOa is photolysis to HO_2 (R3), and JHCHOb is photolysis to H_2 (R2).

modeled HCHO is 26%. As in the lower troposphere, Cl (8%), $j_{HCHO(HCO)}$ (9%), and $j_{HCHO(H2)}$ (17%) each contribute significantly to the overall uncertainty. Uncertainty in acetaldehyde measurements leads to a 12% uncertainty in modeled HCHO.

In addition, the analysis here neglects heterogeneous chemistry. Aerosol observations during CONTRAST were insufficient to model HCHO heterogeneous chemistry accurately, and the F0AM box model currently does not have the capability to model heterogeneous reactions. Mechanisms to produce HCHO from species dissolved in clouds, such as methanol (Tabazadeh et al., 2004), have been previously suggested. Because we are only modeling air parcels that have not been convectively lofted within 24 h observations and convective transport tends to remove HCHO (e.g., Fried et al., 2016), production within clouds is unlikely to have a large effect on our modeling results. Further investigation into the effects of heterogeneous chemistry on HCHO production in the TWP is clearly warranted, however.

Low mixing ratios of HCHO in the UT and their associated uncertainties could also contribute to the differences between measurement and the model. Despite the 25 L min^{-1} flow rate through the inlet, it is possible that trace amounts of HCHO do adsorb and later desorb on the inlet tubing. In addition, decomposition of thermally unstable species in the instrument inlet (i.e., measurement artifacts) could contribute to this difference. One such species, MPN could decompose to the methyl peroxy radical under the warm inlet conditions and convert to HCHO. Based on an estimated 15 pptv of MPN, taken from the box model, we estimate an upper limit of ~2 pptv HCHO production from MPN decomposition, a value well within the measurement uncertainty. Recent laboratory studies also suggest a possible ozone interference at high O_3. For a typical UT value of 20 ppbv, however, this interference is also on the order of 2 pptv.

Total formaldehyde measurement uncertainty in the UT is on the order of 30 pptv (20 pptv + 10%), suggesting that any measurement/model differences less than 30 pptv could be attributed to measurement uncertainty. Further, as described in section 2.1.1, observations from ISAF are systematically higher with respect to observations from the DFGAS instrument, in some cases by more than 30 pptv in the UT, indicating that there could be some instrumental bias. Because there were frequently observations on the order of 20 to 40 pptv in the Southern Hemisphere and between Guam and Hawaii (see Figure S4), it is unlikely that this potential high

bias is greater than 20 pptv. The measurement uncertainty, combined with this possible bias, and the 26% uncertainty in modeled HCHO yield a total uncertainty of ~40 pptv, which is insufficient to explain the 50–60 pptv difference between observed and modeled values.

The reaction of CH_3O_2 with OH has been suggested as a potentially important CH_3O_2 sink in the remote atmosphere (Fittschen et al., 2014) and is not included in the MCM. Including the various production pathways described by Fittschen et al. (2014) with the kinetics described by Assaf et al. (2016), we find that this reaction has no effect on HCHO formation in the UT (Figure S9) and cannot explain the model/measurement discrepancy shown in Figure 6. These results are in agreement with those found by Muller et al. (2016).

Another potential reason for disagreement between observations and the model is a HCHO source not well constrained in the box model. Prather and Jacob (1997) suggest that convective transport of MHP can significantly alter upper tropospheric composition. The atmospheric lifetime of MHP allows it to persist in the UT in comparatively high concentrations for days after convection. To determine the possible impact of convective transport of MHP on HCHO production, we performed an additional box model run in which we constrain the model to average values of all the input parameters from the base run for observations at pressures less than 200 hPa. In addition, the model is then constrained to various mixing ratios of MHP, which was not measured during CONTRAST, ranging from near 0 to 1,000 pptv. The results are shown in Figure S10a and reveal a linear relationship between modeled HCHO and constrained MHP. The measured mean of HCHO at these pressures (72.8 pptv) suggests an upper tropospheric MHP mixing ratio of 105 to 235 pptv, assuming a total uncertainty of 40 pptv. The upper end of this range is consistent with the upper tropospheric (~14 km) MHP values found in the PEM-West campaign and used by Prather and Jacob (1997). In the DC3 campaign conducted over the Central U.S., however, mean values of MHP at these pressure levels were ~100 pptv, consistent with the lower range of the estimate derived here. Further in situ observations of MHP in this region are needed. For the base F0AM model run, the mean MHP mixing ratio at pressures less than 200 hPa is only 5 pptv, with a maximum of 25 pptv. Ambient, photochemical production of MHP from precursors appears to be insufficient to explain the quantities of MHP necessary to reproduce the HCHO observed during CONTRAST. Convective transport of MHP from the lower troposphere is likely one of the driving mechanisms for HCHO production in the UT.

Additional HCHO could also be produced from photolysis of glyoxal (HCOHCO), another species not well constrained in the box model. In the tropical free troposphere, 3 to 20 pptv glyoxal has recently been observed over the tropical eastern Pacific (TEP), where about half of the glyoxal column (2.6×10^{14} cm^{-2}) resides at altitudes above 2 km (Volkamer et al., 2015). The box model, however, only yields an average of 0.1 pptv glyoxal in the UT. While the AMAX DOAS instrument has, in principle, the capability to measure glyoxal, the spectra were not evaluated for that substance during CONTRAST. We have constrained the F0AM box model to glyoxal mixing ratios from 0 to 20 pptv, with the same setup as described above for MHP, finding that 10 pptv of glyoxal in the UT can provide an additional 5 pptv of HCHO (Figure S10b). Production of HCHO from glyoxal cannot explain the entire discrepancy between observations and the model but could provide as high as ~10% of the total observed HCHO in the UT, assuming a similar distribution as seen in the TEP. Convective transport, as with MHP, could be a mechanism to increase glyoxal mixing ratios in the UT. The high solubility of glyoxal, with a Henry's law constant on the order of 10^5 M atm^{-1} or higher (Sander, 2015), along with its short atmospheric lifetime of ~1 h in the tropics (Fu et al., 2008), suggests the need for transport of its precursors as well. Further, vertically resolved observations of glyoxal in the TWP are needed to clarify its role in HCHO production.

Finally, it is possible that the box model is not well constrained to ethene. We use output from CAM-Chem to constrain the box model runs, but it has been suggested that ethene, like acetaldehyde, is emitted by the oceans (Horowitz et al., 2003). Convective transport of ethene, which has a lifetime on the order of 1–2 days, could therefore perturb UT HCHO. Using a box model analysis analogous to that done with MHP and glyoxal, 200 pptv of ethene in the UT, a value consistent with surface observations from previous campaigns, would produce an additional 15 pptv of HCHO, suggesting that this species, along with MHP and to a lesser extent glyoxal, could explain the measurement model difference.

3.3.2. Chemical Sources and Sinks of HCHO

To determine the relative importance of a given compound to HCHO formation, additional zero-out box model runs in which the model was not constrained to a given species were also performed. The percent

change in HCHO mixing ratio between these runs and the base runs are shown in Figure 9a. In the case of acetaldehyde, the model was also not constrained to the higher-order aldehydes, propanal, and butanal, which can form small concentrations of acetaldehyde photochemically. In the halogen case, all halogen chemistry was omitted. Nonlinearities in the model chemistry prevent exact determination of the contributions for each species using this method, but the relative importance can be determined. This is particularly true at pressures greater than 500 hPa, where the box model accurately captures HCHO mixing ratios to within ~10%. In the UT, where observations can be a factor of 4 (50–60 pptv) higher than the model, the percentage contributions for individual species are less certain, but nonetheless, important information can still be inferred.

In agreement with previous studies, CH_4 oxidation is the primary contributor to HCHO production, accounting for between 55 and 65% of total HCHO throughout the tropospheric column. As discussed in section 3.3.1, MHP convectively transported from the surface is a potential contributor to upper tropospheric HCHO, suggesting that the contribution from CH_4, a MHP precursor, at these pressures is even greater than indicated in Figure 9. MHP has an atmospheric lifetime on the order of several days, so even in the absence of recent convection, it could still contribute to HCHO production. Despite the remote location, HCHO production from VOCs is also significant. Acetaldehyde is responsible for 10 to 15% of total production of HCHO in the lower troposphere. At pressures less than 200 hPa, contributions to HCHO by acetaldehyde can still be substantial, reaching as high as 20 pptv, a significant fraction of total HCHO. Acetaldehyde is primarily removed by photolysis and OH oxidation and has an atmospheric lifetime on the order of 1 day in the UT, implying that the observed acetaldehyde must be produced locally, likely from photochemical production in the ocean surface layer and the subsequent transport to the UT through deep convection or from in situ production in the atmosphere. While a significant portion of acetaldehyde would be removed after 1 day of convection, the observed mixing ratios in the UT suggest that at least some of this species could remain after 24 h. Contributions from methanol and acetone are generally on the order of 5%, while production of HCHO from isoprene is negligible, except in air parcels observed near Papua New Guinea. Finally, as described in the previous section, glyoxal could contribute as much as 10 pptv of HCHO.

Halogens both produce and remove HCHO but act as a net source, generating between 10 and 50 pptv of HCHO throughout the tropospheric column, primarily from methane oxidation. This translates to less than 10% of HCHO production in the lower troposphere but is the second most important source after CH_4 at 150 hPa. This increase in the halogen impact on HCHO is dependent on the relative importance of the reaction of Cl with CH_4 as compared to OH oxidation. At pressures between the surface and 450 hPa, Cl only accounts for between 6 to 7% of the loss of CH_4 (Figure 9c). In the UT, however, this fraction doubles to 13%. The low abundance of OH in the UT, driven by cold temperatures and the resultant low water vapor, increases the importance of methane oxidation by Cl. This trend is in agreement with Saiz-Lopez and Fernandez (2016), who determined that the cold temperatures and low ozone abundances in the UT enhance the atmospheric impacts of atomic chlorine, bromine, and iodine within the tropical rings of atomic halogens.

In contrast, halogen chemistry is relatively unimportant for HCHO removal, accounting for only 1 to 2% of HCHO destruction throughout the tropospheric column (Figure 9b), in agreement with previous studies (Sherwen et al., 2016; Wagner et al., 2002). In the lower troposphere, the remaining chemical removal of HCHO is almost evenly distributed among the two photolytic pathways and reaction with OH. As with CH_4 removal, the reaction of HCHO with OH decreases in importance with decreasing pressure as OH concentrations decrease. At 150 hPa, this reaction accounts for only 8% of total HCHO removal, while the photolysis reactions (R2) and (R3) account for 55% and ~35%, respectively.

3.4. Formaldehyde in Global Models

We now evaluate the representation of the HCHO distribution in both a CTM and models that participated in the CCMI experiment. Using the results from the previous sections, we compare the modeled distribution to the CONTRAST observations and use the results from the box modeling analysis to determine the major drivers in any discrepancies between measurement and model.

3.4.1. CAM-Chem

Figures 7b and 10 compare observed HCHO and that modeled by CAM-Chem run in specified dynamics mode (i.e., the model was nudged by the analyzed meteorological field for the time period of the CONTRAST experiment). As with the photochemical box model, CAM-Chem consistently underestimates

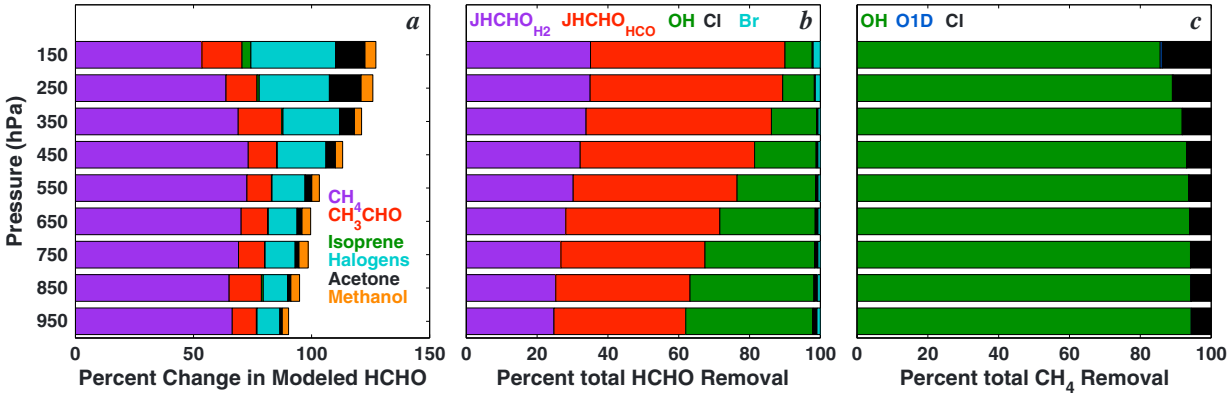

Figure 9. (a) Estimate of the relative contribution of the indicated species to HCHO production at various pressures. Value for each species is determined by calculating the difference in modeled HCHO from the F0AM base box model run from a second run, in which the box model is not constrained to the indicated species. The halogens case removes all halogen chemistry from the model. Totals do not add up to 100% because of additional minor sources, nonlinearities in the chemistry, and interactions among the various sources. (b) Percent of HCHO lost to each sink as calculated by the F0AM model. Photolysis to HO_2 (purple), photolysis to H_2 (red), reaction with OH (green), Cl (black), and Br (cyan). (c) Same as Figure 9b except for CH_4. Reaction with OH (green), O^1D (blue), and Cl (black). Data are sorted into 100 hPa pressure bins and averaged over all modeled data points.

HCHO throughout the tropospheric column. In contrast with the box model results, however, several modeled values at low pressures lie above the 1:1 line. In the UT, at pressures less than 300 hPa, the model underestimates observed HCHO by ~34 pptv, or approximately a factor of 2 (Figure 10). This is on the order of the ISAF measurement uncertainty at these low mixing ratios. At pressures greater than 500 hPa, however, this difference increases to between 100 and 200 pptv, suggesting errors in the model. A thorough analysis of the HCHO sources and sinks in CAM-Chem is needed to discern the cause of this consistent underestimate in the lower troposphere.

First, we investigate the representation of the HCHO precursors acetaldehyde, methane, methanol, and acetone in CAM-Chem (Figures 11c–11f). CAM-Chem significantly underestimates acetaldehyde mixing ratios, the second most important HCHO precursor in the TWP, with a modeled to measured binned ratio of 0.11 ± 0.17. CAM-Chem shows little variation in acetaldehyde mixing ratio throughout the tropospheric column, likely

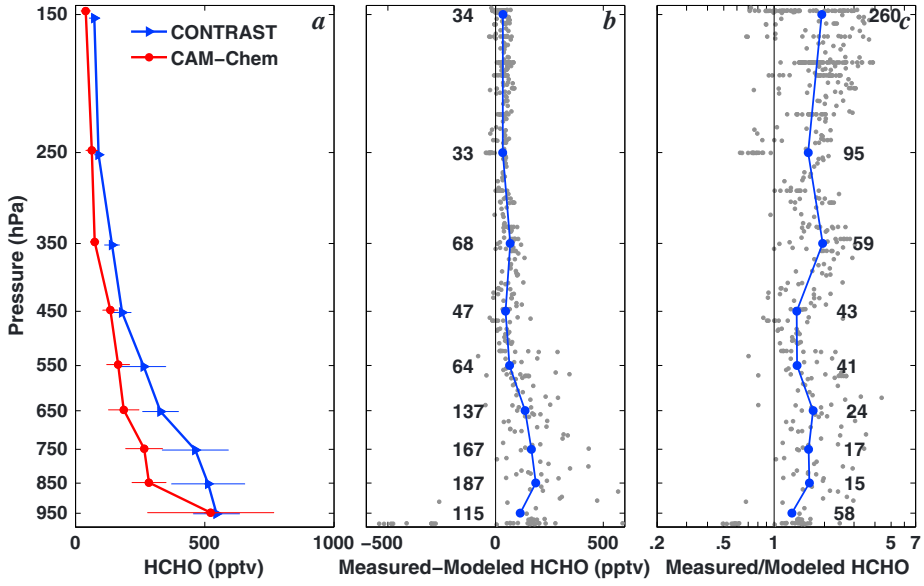

Figure 10. Same as Figure 6 except for CONTRAST observations and model output from CAM-Chem interpolated to the CONTRAST flight track.

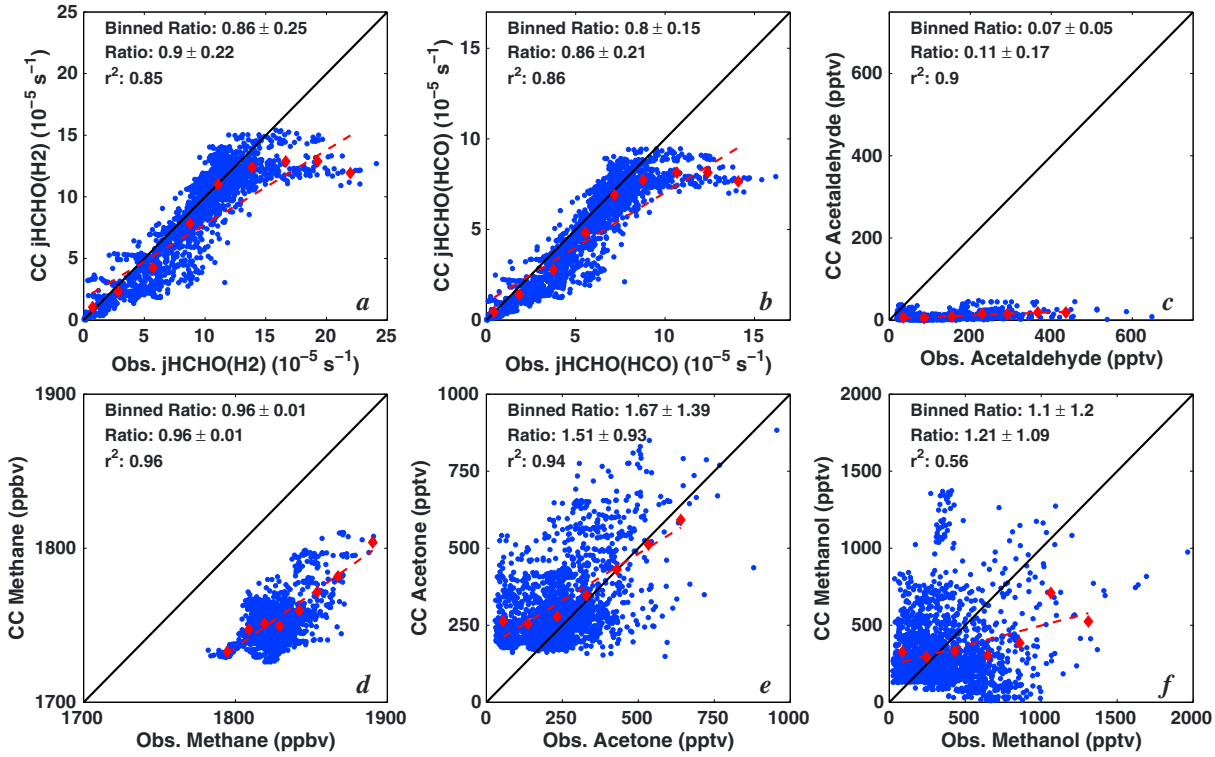

Figure 11. Regression of observed parameters to the corresponding modeled value from CAM-Chem, indicated as CC, along the flight track (blue): (a) photolysis of HCHO to H_2, (b) photolysis of HCHO to HCO, (c) acetaldehyde, (d) methane, (e) acetone, and (f) methanol. Data are for flights RF04–RF15 for observations made between 20°N and 20°S. The red diamonds are the mean value of the data separated into 10 bins with an equal number of observations. The 1:1 lines are shown in black, while the lines of best fit for the binned data, found using a linear least squares regression, are shown in red. The r^2 for each regression and the mean and standard deviation of the ratio of modeled to observed species for all data and for the binned data are also shown.

from a combination of omission of oceanic acetaldehyde emissions and misrepresentation of secondary production (Nicely et al., 2016; Read et al., 2012). The mean modeled to measured binned ratios of methane, methanol, and acetone are 0.96 ± 0.004, 1.32 ± 1.05, and 1.64 ± 1.11, respectively. The 4% low bias in methane, resulting from methane emissions being taken from the RCP6.0 forecast, cannot explain the factor of 2 underestimate by CAM-Chem. While the difference between observations and the model are larger for methanol and acetone, the box model analysis described earlier shows that both species contribute less than 10% to total HCHO formation at most pressure levels. It is unlikely that the errors in these species can explain the consistent underestimate of HCHO within CAM-Chem.

Comparisons between observations and model output of the two HCHO photolytic pathways are shown in Figures 11a and 11b. For $j_{HCHO(H2)}$, CAM-Chem only slightly underestimates lower tropospheric values for observed rates between 5 and 12 × 10^{-5} s^{-1}. At photolysis frequencies greater than this value, modeled j_{HCHO} remains relatively constant, while the observations increase to almost 20 × 10^{-5} s^{-1} in some cases. This leads to an average modeled to observed binned ratio of 0.90 ± 0.22. Local maxima in j_{HCHO} likely result from observations over clouds below the GV and the resultant increase in upwelling radiation associated with backscatter from these clouds. The model resolution and convective parameterizations likely preclude CAM-Chem from accurately modeling photolysis frequencies in these instances. Uncertainty in the observed HCHO photolysis rates could further add to this disagreement. Similar results are found for $j_{HCHO(HCO)}$. This underestimate in j_{HCHO}, most pronounced in the UT, suggests that the model is removing HCHO too slowly, potentially compensating for other model errors.

To determine the relative impacts of errors in methane, methanol, acetaldehyde, acetone, and the two formaldehyde photolysis pathways on CAM-Chem modeled HCHO, additional runs of the F0AM box model were performed. Here values of species from CAM-Chem were interpolated to the CONTRAST flight track for all flights. Individual box model runs were performed in which observed values of one of these species were

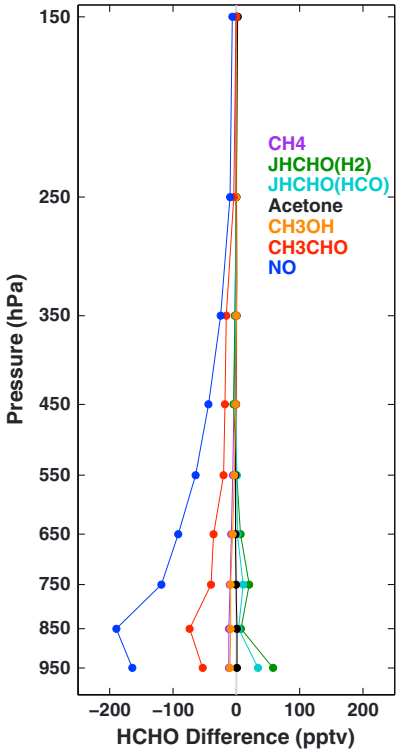

Figure 12. Difference between the F0AM base box model run, constrained with observations from CONTRAST, and box model runs in which observations of the indicated species or photolysis frequency were replaced by output from CAM-Chem run in specified dynamics mode. CAM-Chem values were interpolated to the flight track. Positive (negative) values indicate an increase (decrease) in box-modeled HCHO when using the CAM-Chem output. Median values in 100 hPa pressure bins are shown here.

swapped with the CAM-Chem values. In addition, CAM-Chem significantly underestimates NO_x mixing ratios throughout the troposphere in the CONTRAST domain (Nicely et al., 2016). Formaldehyde formation is strongly influenced by NO, both through its role in converting HO_2 to OH and in converting CH_3O_2 to HCHO (Wolfe, Kaiser, et al., 2016). We therefore performed an additional run constrained to CAM-Chem NO. The difference between these runs and the base F0AM run are shown in Figure 12.

Our box model simulations suggest underestimates in NO and acetaldehyde within CAM-Chem drive the underestimation of HCHO by this CTM. Replacing observed NO with that from CAM-Chem results in reductions of HCHO between 70 and 190 pptv at pressures greater than 500 hPa; replacing observed acetaldehyde results in reductions of HCHO between 20 and 75 pptv. At these pressures, CAM-Chem underestimates HCHO by between 64 and 190 pptv (Figure 10), suggesting that the combination of underestimates of NO and acetaldehyde mixing ratios are more than sufficient to explain the difference between CAM-Chem and observed HCHO. In the UT, the impact on box modeled HCHO of the NO and acetaldehyde swaps, while smaller (between 6 and 45 pptv), still explains a large portion of the model underestimate. Swapping the observations with the CAM-Chem values of other HCHO sources (methane, methanol, and acetone) results in changes in HCHO of less than 10 pptv. Despite the large discrepancies between CAM-Chem and observed HCHO photolysis frequencies in the UT, photolysis swaps only show changes in the lower troposphere. At 950 hPa, box-modeled HCHO increases by 58 and 34 pptv for the H_2 (R2) and HCO (R3) pathways, respectively.

3.4.2. CCMI

While CAM-Chem consistently underestimates HCHO mixing ratios throughout the troposphere, it is important to determine whether this is an issue singularly important to CAM-Chem or if it is a more pervasive problem. The CCMI effort provides an opportunity to evaluate multiple models with monthly averaged output driven by the same set of emissions and climate forcers Morgenstern et al. (2017). As discussed below, the consistent underestimate of HCHO is also found in most of the CCMI models.

Figure 13a shows the vertical profile of HCHO from CONTRAST and 9 CCMI models. Monthly mean output for January and February from the CCMI models has been averaged over the CONTRAST study region (0 to 20°N and 137 to 160°E). Because with the exception of the CHASER model, the other CCMI models are driven by free-running meteorology (i.e., the meteorology of a model year does not necessarily reflect the meteorology of the actual year), we use an average of model years 2001–2010. Total column HCHO in all the models shows little interannual variability (Figure S11), with mean values generally differing by less than ±0.25 cm^{-2}, well within the standard deviation of the observed columns.

As with CAM-Chem, the majority of CCMI models underestimate HCHO mixing ratios in the lower troposphere (Figure 13a). Near the surface, CMAM, CESM1-WACCM, and GEOSCCM are more than a factor of 2 lower than the observations. Also in the lower troposphere, the two setups of EMAC, which are distinguished by the number of vertical levels in the model, are higher than observations near the surface, while CHASER output is nearly indistinguishable from the in situ data. At lower pressures, however, these models tend to underestimate HCHO as well. As discussed below, agreement between GEOSCCM and observations in the midtroposphere likely results from the high lightning NO_x emissions in that model. In the UT, there is generally better agreement between the models and the CONTRAST HCHO, with only CMAM, CESM1-WACCM, and NIWA-UKCA outside of the observed distribution.

When compared to column values, the CCMI models underestimated HCHO by between 4 and 50%. In situ-derived tropospheric column HCHO is compared to the total column HCHO from each of the models in Figure 14. In the region analyzed here, the in situ mean was 5.1 ± 0.76 × 10^{15} cm^{-2}, showing little

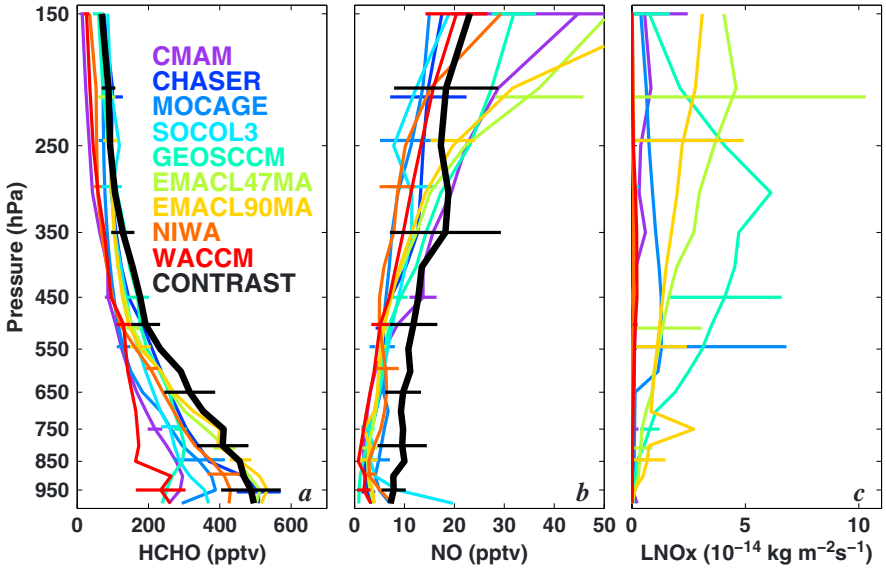

Figure 13. Vertical profiles of (a) HCHO and (b) NO observed during CONTRAST (black) and output from various CCMI models. CONTRAST data are for all daytime flights between 0° and 20°N, have been averaged into 50 hPa pressure bins. NO values are 24 h average values calculated by the DSMACC box model, as described in Nicely et al. (2016). (c) Lightning NO_x emissions from all CCMI models analyzed here except for CHASER, which did not output the variable to the CCMI archive. CCMI output are from the REF-C1 hindcast scenario for all models, in which meteorology is free running, except for CHASER, which uses the REF-C1SD scenario with specified dynamics. Model output is the average of January and February from model years 2001–2010 and has been sampled exclusively over the CONTRAST domain (0° to 20°N and 137° to 160°E). Error bars represent one standard deviation of the mean value. For clarity, some error bars are omitted and others have been offset slightly in the vertical.

variation over the domain. Column HCHO from CCMI varied from 2.5×10^{15} cm^{-2} for CESM1-WACCM to 4.9×10^{15} cm^{-2} for the two setups of EMAC. As with the in situ observations, the majority of models have relatively uniform HCHO distributions in the region, with the exception of MOCAGE and CESM1-WACCM. Both these models demonstrate a strong north/south gradient, with much lower values in the southern portion of the domain, possibly due to influences from Southern Hemispheric air. For CESM1-WACCM, this strong gradient drives the low average over the CONTRAST domain, with average values in the northern portion more in line with the other models.

The lack of NMHC chemistry in some of the models likely contributes to the underestimate of observed HCHO. We have shown that oxygenated VOCs, such as acetaldehyde and glyoxal, can produce 10–20% of the HCHO in the TWP; omitting the emissions and chemistry of these species would therefore lead to model underestimates. CMAM does not include NMHC chemistry, while the only NMHC included in SOCOL3 is isoprene, a species that does not contribute to HCHO production in the TWP. Consistent with this idea, CMAM has the second lowest tropospheric column HCHO of the CCMI models and has significantly lower HCHO over Southeast Asia and the Maritime Continent (Figure 14). Both the distribution of HCHO and the total column HCHO in SOCOL3, however, are comparable to the models with more comprehensive NMHC chemistry. Further, CESM1-WACCM, which includes the chemistry of 17 primary NMHCs and their related oxygenated products, has the lowest total column HCHO of all the models over the CONTRAST study region. This suggests that there are additional drivers to this underestimate than the model chemical mechanisms.

Because the analysis of CAM-Chem shows that low NO in the model is the most likely cause of the model underestimate of HCHO, we also investigate the representation of NO in the CCMI models. Other potential contributors to this error—acetaldehyde, photolysis frequencies, acetone, and methanol—were, at the time of this analysis, not archived by most of the models so cannot be analyzed here. Figure 13b compares the vertical profile of NO from CONTRAST to the various CCMI models. Because of its strong diurnal variability, CONTRAST data are 24 h averaged values, calculated by the Dynamically Simple Model for Atmospheric Chemical Complexity (DSMACC) box model as described in Nicely et al. (2016). Most models underestimate NO throughout the tropospheric column by approximately a factor of 2. This model underestimate is in

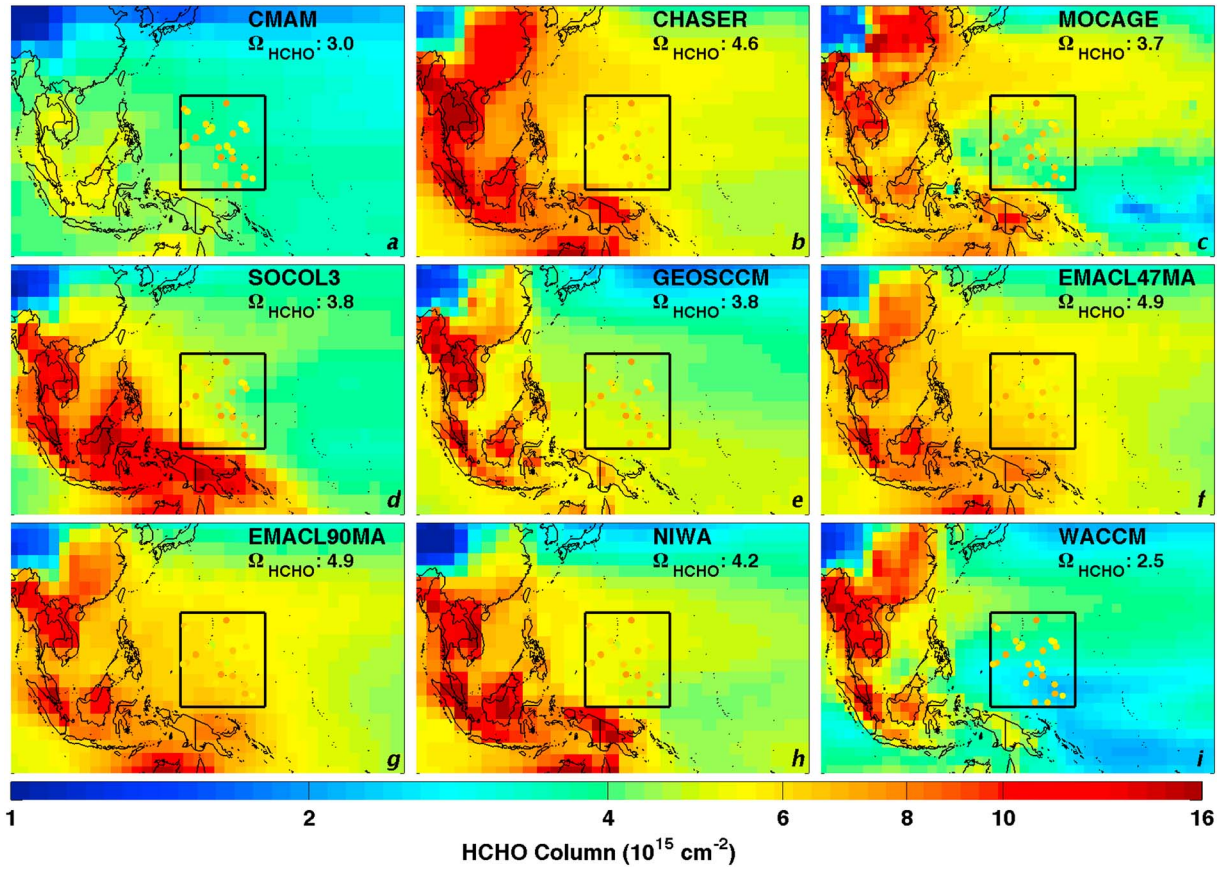

Figure 14. Total column HCHO, averaged over January and February for model years 2001–2010, for each CCMI model analyzed here is shown. The HCHO column (Ω_{HCHO}) averaged over the CONTRAST study region is also indicated. Values have been divided by 10^{15} to increase readability. For comparison to the CCMI models, we limit the CONTRAST study region analyzed to latitudes between 0° and 20°N and longitudes between 137° and 160°E (outlined by the black box) to prevent influence from regions potentially affected by isoprene emissions, such as Papua New Guinea. Tropospheric column HCHO calculated from in situ observations by ISAF are shown as circles. The in situ derived column mean for this region is 5.1×10^{15}.

contrast to previous model comparisons in the region, which found that a majority of CCMs overestimate total NO_x in the region (Brunner et al., 2003). In the lower troposphere, only SOCOL3 overestimates NO near the surface. As was shown with CAM-Chem, underestimates in NO of this magnitude can lead to differences in HCHO on the order of 100 to 200 pptv, suggesting that the low values of NO in the CCMI models could be a cause for the disagreement between the measured and modeled HCHO. For EMAC, which only underestimates observed HCHO columns by ~4%, there must be additional errors in the model, such as a low bias in HCHO photolysis, that compensate for the low NO, which is comparable to that of the other models. To evaluate the drivers of the low HCHO biases in these models more thoroughly, HCHO sources and sinks should be consistently output for all models in future intercomparison projects.

In the UT, CMAM, GEOSCCM, NIWA-UKCA, and the two setups of EMAC show a sharp rise in NO between 200 and 300 hPa. This suggests that the good agreement between measured and modeled HCHO in these models could result from this high NO in the UT. Potential sources of this high NO could be erroneously large production of NO_x from lightning in the CONTRAST domain or incorrect tropopause heights in the model. There was no observational evidence of significant lightning NO_x production over the TWP during CONTRAST (section 3.2). Multiple models, particularly EMAC and GEOSCCM, show production of NO_x from lightning throughout the troposphere. The pronounced increase in upper tropospheric NO in these models likely results from this overproduction of NO_x by lightning. The parameterizations used for lightning NO_x production in these models should be investigated. NO at 150 hPa is also overestimated by the NIWA-UKCA model, although lightning NO_x emissions were several orders of magnitude lower than those in GEOSCCM and

EMAC. In this case, the tropopause height, as determined by the relationship between CO and O_3 (Pan et al., 2004), was significantly lower for NIWA-UKCA (115 ± 0.14 hPa) than for the other CCMI models (multimodel mean without NIWA-UKCA: 80 ± 5.5 hPa). This suggests that the slightly high NO from NIWA-UKCA could result from stratospheric influence due to the low tropopause.

The consistent underestimation of HCHO by all models, both those that participated in CCMI and CAM-Chem, suggests that there are significant shortcomings in the NO_x emissions inventories, VOC emissions, and/or in the chemical mechanisms used in these models. Anderson et al. (2016) showed that biomass burning contributes to high NO_x in the midtroposphere (300 and 700 hPa), while we suggest here (section 3.2) that high NO in the UT likely originates from other anthropogenic sources. Emissions inventories for both these sources should be evaluated to determine their accuracy. Low NO_x emissions would, of course, have implications for the models beyond their effects on HCHO production, including affecting the atmospheric oxidative capacity and ozone production efficiency. The low NO bias could also be a result of the models incorrectly apportioning reactive nitrogen species to long-lived, reservoir species, such as peroxyacetyl nitrate (PAN), which would decrease NO_x abundance. Future field campaigns in the TWP should measure a wider suite of reactive nitrogen compounds to further evaluate these models. In addition, we have shown that the lack of oceanic emissions of acetaldehyde is another likely source of model underestimates of HCHO in the lower troposphere for CAM-Chem. The CCMI models also lack this source and, in some cases, acetaldehyde chemistry altogether. Ethene emissions are potentially underestimated in the models as well, suggesting a need for the implementation of better VOC emissions schemes from oceans in global models.

4. Conclusions

We have used observations from the CONTRAST field campaign, conducted during January and February 2014, to evaluate our understanding of the processes controlling the distribution of HCHO in the TWP. Observed HCHO ranged from ~500 pptv near the surface to ~75 pptv in the UT, exhibiting larger mixing ratios than observed in previous studies in the TWP. Air parcels that had been convected within 24 h of observation had a shift in HCHO distributions, with the median of the convectively influenced air 33% (22 pptv) higher than the aged air and a factor of 10 (~25 pptv) higher acetaldehyde than aged parcels, suggesting that convection in the West Pacific warm pool perturbs upper tropospheric HCHO composition through transport of HCHO and through transport of precursors, such as acetaldehyde. The aged air parcels, which have higher concentrations of anthropogenic pollutants, such as NO and benzene, shift the HO_x balance in the UT, increasing OH by a factor of 1.4. Remarkably low NO mixing ratios were observed in air that had seen recent convection, indicating little or no influence from lightning.

A photochemical box model, constrained to observations made during CONTRAST, generally agreed with observations within 10% at pressures greater than 500 hPa, suggesting that HCHO chemistry is well understood and that convective outflow does not significantly perturb HCHO in the lower half of the troposphere. In the UT, however, observations of HCHO were a factor of 4 (50 to 60 pptv absolute difference) higher than box model output. Thirty to 40 pptv of this difference could be explained by a combination of model and HCHO measurement uncertainties, including potential measurement artifacts on the order of 20 pptv, a value consistent with the measurement uncertainty. Convective transport of various HCHO precursors, including MHP, ethene, and glyoxal, can also reasonably explain the disagreement between measurement and model. Further observations with multiple HCHO instruments and measurements of these missing precursors are needed to definitively determine the source of this discrepancy. Box model analysis shows that CH_4 and acetaldehyde are the dominant HCHO precursors in the TWP, with minor contributions from acetone and methanol.

Observations of HCHO in the remote Pacific in future campaigns, such as the Atmospheric Tomography mission, are needed to determine the seasonality of the HCHO distribution as well as its spatial variability across the Pacific basin. In situ measurements of MHP in the region would provide additional evidence of the impacts of convective transport in the region and further constrain the HCHO budget in the UT. Measurements of glyoxal, throughout the tropospheric column in the TWP but particularly in the UT, are also needed to determine whether the species is abundant enough to contribute significantly to the HCHO budget.

Output of HCHO from the CAM-Chem model and nine additional models that participated in CCMI was compared to CONTRAST observations, and it was shown that all models underestimate HCHO throughout the troposphere. For CAM-Chem, consistent underestimation of NO and acetaldehyde is the primary driver of the difference between the observations and the model. Underestimates in NO, as well as limitations with the model chemical mechanisms, likely drive errors in the CCMI models as well.

Additional model runs including oceanic emissions of acetaldehyde are needed to determine whether this increases agreement between measured and modeled HCHO in the lower troposphere. Observations of NO, NO_2, and other reactive nitrogen species, such as PAN and alkyl nitrates, in the TWP are needed to evaluate the partitioning of nitrogen in CCMs and to determine whether potential errors in this partitioning are the cause of the nearly universal underestimate in tropospheric NO. The NO_x emissions inventories used in these models, both for biomass burning and fossil fuels, should be evaluated to determine their accuracy, as the underestimate in NO could also be the result of incorrect emissions. Lightning NO_x parameterizations in those models that suggest significant emissions in the TWP during winter, particularly EMAC and GEOSCCM, should also be investigated, since observations during CONTRAST suggested minimal lightning NO_x production. Finally, evaluation of HCHO in future modeling intercomparison projects would be facilitated by the requirement that all models output global fields of HCHO precursors and sinks, allowing a more thorough investigation with a box modeling analysis similar to that performed here with CAM-Chem.

Acknowledgments

We would like to thank H. Fischer for insight into the role of MHP, the CONTRAST field team for help with field operations, and the pilots and crews of the CAST BAe-146 and CONTRAST Gulfstream V aircrafts for their dedication and professionalism. CAST was funded by the Natural Environment Research Council; CONTRAST was funded by the National Science Foundation (grant NSF-AGS-1261740). A number of the U.S.-based investigators also benefitted from the support of NASA. Work conducted at the University of Maryland was supported, in part, by the NASA Modeling and Analysis Program under NNH12ZDA001N-MAP. G. M. W., D. C. A., and T. F. H. received supported from the NASA Upper Atmospheric Research Program under NNH12ZDA001N-UACO. J. M. N. was supported by an appointment to the NASA Postdoctoral Program at the NASA Goddard Space Flight Center, administered by Universities Space Research Association under contract with NASA. We would like to acknowledge high-performance computing support from Yellowstone (ark:/85065/d7wd3xhc) provided by NCAR's Computational and Information Systems Laboratory. NCAR is sponsored by the National Science Foundation. CONTRAST data are publicly available for all researchers and can be obtained at http://data.eol.ucar.edu/master_list/?project = CONTRAST. The CAM-Chem model simulations are available upon request to the lead author (dca54@drexel.edu). CCMI output for all models except CESM1-WACCM is available at badc.nerc.ac.uk; CESM1-WACCM output is available at www.earthsystemgrid.org. We acknowledge the joint WCRP SPARC/IGAC Chemistry-Climate Model Initiative (CCMI) for organizing and coordinating the model data analysis activity and the British Atmospheric Data Centre (BADC) for collecting and archiving the CCMI model output. O. M. acknowledges funding by the Royal Society of New Zealand (grant 12-NIW-006). The authors wish to acknowledge the contribution of NeSI high-performance computing facilities to the results of this research. New Zealand's national facilities are provided by the NZ eScience Infrastructure and funded jointly by NeSI's collaborator institutions and through the Ministry of Business, Innovation & Employment's Research Infrastructure programme: URL https://www.nesi.org.nz. The EMAC simulations have been performed at the German Climate Computing Centre (DKRZ) through support from the Bundesministerium für Bildung und Forschung (BMBF). DKRZ and its scientific steering committee are

References

Akagi, S. K., Yokelson, R. J., Wiedinmyer, C., Alvarado, M. J., Reid, J. S., Karl, T., … Wennberg, P. O. (2011). Emission factors for open and domestic biomass burning for use in atmospheric models. *Atmospheric Chemistry and Physics*, *11*(9), 4039–4072. https://doi.org/10.5194/acp-11-4039-2011

Amato, P., Demeer, F., Melaouhi, A., Fontanella, S., Martin-Biesse, A.-S., Sancelme, M., … Delort, A.-M. (2007). A fate for organic acids, formaldehyde and methanol in cloud water: Their biotransformation by micro-organisms. *Atmospheric Chemistry and Physics*, *7*(15), 4159–4169. https://doi.org/10.5194/acp-7-4159-2007

Anderson, D. C., Nicely, J. M., Salawitch, R. J., Canty, T. P., Dickerson, R. R., Hanisco, T. F., … Weinheimer, A. J. (2016). A pervasive role for biomass burning in tropical high ozone/low water structures. *Nature Communications*, *7*, 10267. https://doi.org/10.1038/ncomms10267

Andreae, M. O., & Merlet, P. (2001). Emission of trace gases and aerosols from biomass burning. *Global Biogeochemical Cycles*, *15*(4), 955–966. https://doi.org/10.1029/2000GB001382

Apel, E. C., Emmons, L. K., Karl, T., Flocke, F., Hills, A. J., Madronich, S., … Riemer, D. D. (2010). Chemical evolution of volatile organic compounds in the outflow of the Mexico City Metropolitan area. *Atmospheric Chemistry and Physics*, *10*(5), 2353–2375. https://doi.org/10.5194/acp-10-2353-2010

Assaf, E., Song, B., Tomas, A., Schoemaecker, C., & Fittschen, C. (2016). Rate constant of the reaction between CH3O2 radicals and OH radicals revisited. *The Journal of Physical Chemistry A*, *120*(45), 8923–8932. https://doi.org/10.1021/acs.jpca.6b07704

Atkinson, R., Baulch, D. L., Cox, R. A., Crowley, J. N., Hampson, R. F., Hynes, R. G., & Troe, J. (2006). Evaluated kinetic and photochemical data for atmospheric chemistry: Volume II—Gas phase reactions of organic species. *Atmospheric Chemistry and Physics*, *6*(11), 3625–4055. https://doi.org/10.5194/acp-6-3625-2006

Ayers, G. P., Gillett, R. W., Granek, H., deServes, C., & Cox, R. A. (1997). Formaldehyde production in clean marine air. *Geophysical Research Letters*, *24*(4), 401–404. https://doi.org/10.1029/97GL00123

Baidar, S., Oetjen, H., Coburn, S., Dix, B., Ortega, I., Sinreich, R., & Volkamer, R. (2013). The CU airborne MAX-DOAS instrument: Vertical profiling of aerosol extinction and trace gases. *Atmospheric Measurement Techniques*, *6*(3), 719–739. https://doi.org/10.5194/amt-6-719-2013

Barnes, I., Hjorth, J., & Mihalopoulos, N. (2006). Dimethyl sulfide and dimethyl Sulfoxide and their oxidation in the atmosphere. *Chemical Reviews*, *106*(3), 940–975. https://doi.org/10.1021/cr020529+

Barth, M. C. (2003). Summary of the cloud chemistry modeling intercomparison: Photochemical box model simulation. *Journal of Geophysical Research*, *108*(D7), 4214. https://doi.org/10.1029/2002JD002673

Bell, N., Hsu, L., Jacob, D. J., Schultz, M. G., Blake, D. R., Butler, J. H., … Maier-Reimer, E. (2002). Methyl iodide: Atmospheric budget and use as a tracer of marine convection in global models. *Journal of Geophysical Research*, *107*(D17), 4340. https://doi.org/10.1029/2001JD001151

Bergman, J. W., Jensen, E. J., Pfister, L., & Yang, Q. (2012). Seasonal differences of vertical-transport efficiency in the tropical tropopause layer: On the interplay between tropical deep convection, large-scale vertical ascent, and horizontal circulations. *Journal of Geophysical Research*, *117*, D05302. https://doi.org/10.1029/2011JD016992

Blake, N. J. (2003). NMHCs and halocarbons in Asian continental outflow during the transport and chemical evolution over the Pacific (TRACE-P) field campaign: Comparison with PEM-West B. *Journal of Geophysical Research*, *108*(D20), 8806. https://doi.org/10.1029/2002JD003367

Borbon, A., Ruiz, M., Bechara, J., Aumont, B., Chong, M., Huntrieser, H., … Perros, P. E. (2012). Transport and chemistry of formaldehyde by mesoscale convective systems in West Africa during AMMA 2006. *Journal of Geophysical Research*, *117*, D12301. https://doi.org/10.1029/2011JD017121

Brunner, D., Staehelin, J., Rogers, H. L., Köhler, M. O., Pyle, J. A., Hauglustaine, D., … Sausen, R. (2003). An evaluation of the performance of chemistry transport models by comparison with research aircraft observations. Part 1: Concepts and overall model performance. *Atmospheric Chemistry and Physics*, *3*(5), 1609–1631. https://doi.org/10.5194/acp-3-1609-2003

Cazorla, M., Wolfe, G. M., Bailey, S. A., Swanson, A. K., Arkinson, H. L., & Hanisco, T. F. (2015). A new airborne laser-induced fluorescence instrument for in situ detection of formaldehyde throughout the troposphere and lower stratosphere. *Atmospheric Measurement Techniques*, *8*(2), 541–552. https://doi.org/10.5194/amt-8-541-2015

Cecil, D. J., Buechler, D. E., & Blakeslee, R. J. (2014). Gridded lightning climatology from TRMM-LIS and OTD: Dataset description. *Atmospheric Research*, *135–136*, 404–414. https://doi.org/10.1016/j.atmosres.2012.06.028

gratefully acknowledged for providing the HPC and data archiving resources for this consortial project ESCiMo (Earth System Chemistry integrated Modelling).

Chen, D., Huey, L. G., Tanner, D. J., Salawitch, R. J., Anderson, D. C., Wales, P. A., … Wolfe, G. M. (2016). Airborne measurements of BrO and the sum of HOBr and Br2 over the tropical West Pacific from 1 to 15 km during the CONvective TRansport of Active Species in the Tropics (CONTRAST) experiment. *Journal of Geophysical Research: Atmospheres*, *121*(20), 12,560–12,578. https://doi.org/10.1002/2016JD025561

Chen, G. (2017). Intercomparison results: NASA DC-8 Intraplatform comparison (https://www-air.larc.nasa.gov/missions/dc3-seac4rs/comparisons/index.html), edited.

Coburn, S., Ortega, I., Thalman, R., Blomquist, B., Fairall, C. W., & Volkamer, R. (2014). Measurements of diurnal variations and eddy covariance (EC) fluxes of glyoxal in the tropical marine boundary layer: Description of the fast LED-CE-DOAS instrument. *Atmospheric Measurement Techniques*, *7*(10), 3579–3595. https://doi.org/10.5194/amt-7-3579-2014

Crosson, E. R. (2008). A cavity ring-down analyzer for measuring atmospheric levels of methane, carbon dioxide, and water vapor. *Applied Physics B: Lasers and Optics*, *92*(3), 403–408. https://doi.org/10.1007/s00340-008-3135-y

De Smedt, I., Stavrakou, T., Hendrick, F., Danckaert, T., Vlemmix, T., Pinardi, G., … Van Roozendael, M. (2015). Diurnal, seasonal and long-term variations of global formaldehyde columns inferred from combined OMI and GOME-2 observations. *Atmospheric Chemistry and Physics*, *15*(21), 12,519–12,545. https://doi.org/10.5194/acp-15-12519-2015

DiGangi, J. P., Boyle, E. S., Karl, T., Harley, P., Turnipseed, A., Kim, S., … Keutsch, F. N. (2011). First direct measurements of formaldehyde flux via eddy covariance: Implications for missing in-canopy formaldehyde sources. *Atmospheric Chemistry and Physics*, *11*(20), 10,565–10,578. https://doi.org/10.5194/acp-11-10565-2011

Economou, C., & Mihalopoulos, N. (2002). Formaldehyde in the rainwater in the eastern Mediterranean: Occurrence, deposition and contribution to organic carbon budget. *Atmospheric Environment*, *36*(8), 1337–1347. https://doi.org/10.1016/s1352-2310(01)00555-6

Fernandez, R. P., Salawitch, R. J., Kinnison, D. E., Lamarque, J. F., & Saiz-Lopez, A. (2014). Bromine partitioning in the tropical tropopause layer: Implications for stratospheric injection. *Atmospheric Chemistry and Physics*, *14*(24), 13,391–13,410. https://doi.org/10.5194/acp-14-13391-2014

Fittschen, C., Whalley, L. K., & Heard, D. E. (2014). The reaction of CH_3O_2 radicals with OH radicals: A neglected sink for CH_3O_2 in the remote atmosphere. *Environmental Science & Technology*, *48*(14), 7700–7701. https://doi.org/10.1021/es502481q

Fortems-Cheiney, A., Chevallier, F., Pison, I., Bousquet, P., Saunois, M., Szopa, S., … Fried, A. (2012). The formaldehyde budget as seen by a global-scale multi-constraint and multi-species inversion system. *Atmospheric Chemistry and Physics*, *12*(15), 6699–6721. https://doi.org/10.5194/acp-12-6699-2012

Franco, B., Hendrick, F., Van Roozendael, M., Müller, J.-F., Stavrakou, T., Marais, E. A., … Mahieu, E. (2015). Retrievals of formaldehyde from ground-based FTIR and MAX-DOAS observations at the Jungfraujoch station and comparisons with GEOS-Chem and IMAGES model simulations. *Atmospheric Measurement Techniques*, *8*(4), 1733–1756. https://doi.org/10.5194/amt-8-1733-2015

Fried, A., Barth, M. C., Bela, M., Weibring, P., Richter, D., Walega, J., … Woods, S. (2016). Convective transport of formaldehyde to the upper troposphere and lower stratosphere and associated scavenging in thunderstorms over the central United States during the 2012 DC3 study. *Journal of Geophysical Research: Atmospheres*, *121*, 7430–7460. https://doi.org/10.1002/2015JD024477

Fried, A., Cantrell, C., Olson, J., Crawford, J. H., Weibring, P., Walega, J., … Sachse, G. (2011). Detailed comparisons of airborne formaldehyde measurements with box models during the 2006 INTEX-B and MILAGRO campaigns: Potential evidence for significant impacts of unmeasured and multi-generation volatile organic carbon compounds. *Atmospheric Chemistry and Physics*, *11*(22), 11,867–11,894. https://doi.org/10.5194/acp-11-11867-2011

Fried, A., Crawford, J., Olson, J., Walega, J., Potter, W., Wert, B., … Carmichael, G. R. (2003). Airborne tunable diode laser measurements of formaldehyde during TRACE-P: Distributions and box model comparisons. *Journal of Geophysical Research*, *108*(D20), 8798. https://doi.org/10.1029/2003JD003451

Fried, A., Olson, J. R., Walega, J. G., Crawford, J. H., Chen, G., Weibring, P., … Millet, D. B. (2008). Role of convection in redistributing formaldehyde to the upper troposphere over North America and the North Atlantic during the summer 2004 INTEX campaign. *Journal of Geophysical Research*, *113*, D17306. https://doi.org/10.1029/2007JD009760

Friedfeld, S., Fraser, M., Ensor, K., Tribble, S., Rehle, D., Leleux, D., & Tittel, F. (2002). Statistical analysis of primary and secondary atmospheric formaldehyde. *Atmospheric Environment*, *36*(30), 4767–4775. https://doi.org/10.1016/s1352-2310(02)00558-7

Frost, G. J., Fried, A., Lee, Y.-. N., Wert, B., Henry, B., Drummond, J. R., … Williams, J. (2002). Comparisons of box model calculations and measurements of formaldehyde from the 1997 North Atlantic Regional Experiment. *Journal of Geophysical Research*, *107*(D8), 4060. https://doi.org/10.1029/2001JD000896

Fu, T.-M., Jacob, D. J., Wittrock, F., Burrows, J. P., Vrekoussis, M., & Henze, D. K. (2008). Global budgets of atmospheric glyoxal and methylglyoxal, and implications for formation of secondary organic aerosols. *Journal of Geophysical Research*, *113*, D15303. https://doi.org/10.1029/2007JD009505

Fueglistaler, S., Dessler, A. E., Dunkerton, T. J., Folkins, I., Fu, Q., & Mote, P. W. (2009). Tropical tropopause layer. *Reviews of Geophysics*, *47*, RG1004. https://doi.org/10.1029/2008RG000267

Fueglistaler, S., Dessler, A. E., Dunkerton, T. J., Folkins, I., Fu, Q., & Mote, P. W. (2009). Tropical tropopause layer. *Reviews of Geophysics*, *47*, RG1004. https://doi.org/10.1029/2008RG000267

Fuelberg, H. E. (2003). Meteorological conditions and transport pathways during the transport and chemical evolution over the Pacific (TRACE-P) experiment. *Journal of Geophysical Research*, *108*(D20), 8782. https://doi.org/10.1029/2002jd003092

Gao, R. S., Rosenlof, K. H., Fahey, D. W., Wennberg, P. O., Hintsa, E. J., & Hanisco, T. F. (2014). OH in the tropical upper troposphere and its relationships to solar radiation and reactive nitrogen. *Journal of Atmospheric Chemistry*, *71*(1), 55–64. https://doi.org/10.1007/s10874-014-9280-2

Garcia, A. R., Volkamer, R., Molina, L. T., Molina, M. J., Samuelson, J., Mellqvist, J., … Kolb, C. E. (2006). Separation of emitted and photochemical formaldehyde in Mexico City using a statistical analysis and a new pair of gas-phase tracers. *Atmospheric Chemistry and Physics*, *6*(12), 4545–4557. https://doi.org/10.5194/acp-6-4545-2006

Gerbig, C., Schmitgen, S., Kley, D., Volz-Thomas, A., Dewey, K., & Haaks, D. (1999). An improved fast-response vacuum-UV resonance fluorescence CO instrument. *Journal of Geophysical Research*, *104*(D1), 1699–1704. https://doi.org/10.1029/1998JD100031

González Abad, G., Liu, X., Chance, K., Wang, H., Kurosu, T. P., & Suleiman, R. (2015). Updated Smithsonian Astrophysical Observatory Ozone Monitoring Instrument (SAO OMI) formaldehyde retrieval. *Atmospheric Measurement Techniques*, *8*(1), 19–32. https://doi.org/10.5194/amt-8-19-2015

González Abad, G., Vasilkov, A., Seftor, C., Liu, X., & Chance, K. (2016). Smithsonian Astrophysical Observatory Ozone Mapping and Profiler Suite (SAO OMPS) formaldehyde retrieval. *Atmospheric Measurement Techniques*, *9*(7), 2797–2812. https://doi.org/10.5194/amt-9-2797-2016

Grosjean, D., Grosjean, E., & Gertler, A. W. (2001). On-road emissions of carbonyls from light-duty and heavy-duty vehicles. *Environmental Science & Technology*, *35*(1), 45–53. https://doi.org/10.1021/es001326a

Guth, J., Josse, B., Marecal, V., Joly, M., & Hamer, P. (2016). First implementation of secondary inorganic aerosols in the MOCAGE version R2.15.0 chemistry transport model. *Geoscientific Model Development*, *9*(1), 137–160. https://doi.org/10.5194/gmd-9-137-2016

Harris, N. R. P., Carpenter, L. J., Lee, J. D., Vaughan, G., Filus, M. T., Jones, R. L., … Pyle, J. A. (2016). Coordinated Airborne Studies in the Tropics (CAST). *Bulletin of the American Meteorological Society*, *98*(1), 145–162. https://doi.org/10.1175/bams-d-14-00290.1

Heikes, B., Snow, J., Egli, P., O'Sullivan, D., Crawford, J., Olson, J., … Blake, D. (2001). Formaldehyde over the central Pacific during PEM-Tropics B. *Journal of Geophysical Research: Atmospheres*, *106*(D23), 32,717–32,731. https://doi.org/10.1029/2001JD900012

Holzinger, R., Warneke, C., Hansel, A., Jordan, A., Lindinger, W., Scharffe, D. H., … Crutzen, P. J. (1999). Biomass burning as a source of formaldehyde, acetaldehyde, methanol, acetone, acetonitrile, and hydrogen cyanide. *Geophysical Research Letters*, *26*(8), 1161–1164. https://doi.org/10.1029/1999GL900156

Horowitz, L. W., Walters, S., Mauzerall, D. L., Emmons, L. K., Rasch, P. J., Granier, C., … Granier, C. (2003). A global simulation of tropospheric ozone and related tracers: Description and evaluation of MOZART, version 2. *Journal of Geophysical Research*, *108*(D24), 4784. https://doi.org/10.1029/2002JD002853

Huffman, G. J., Bolvin, D. T., Nelkin, E. J., Wolff, D. B., Adler, R. F., Gu, G., … Stocker, E. F. (2007). The TRMM Multisatellite Precipitation Analysis (TMPA): Quasi-global, multiyear, combined-sensor precipitation estimates at fine scales. *Journal of Hydrometeorology*, *8*(1), 38–55. https://doi.org/10.1175/jhm560.1

Jaegle, L., Jacob, D. J., Brune, W. H., Faloona, I., Tan, D., Heikes, B. G., … Shetter, R. E. (2000). Photochemistry of HO_x in the upper troposphere at northern midlatitudes. *Journal of Geophysical Research*, *105*(D3), 3877–3892. https://doi.org/10.1029/1999JD901016

Jaegle, L., Jacob, D. J., Brune, W. H., Tan, D., Faloona, I. C., Weinheimer, A. J., … Sachse, G. W. (1998). Sources of HO_x and production of ozone in the upper troposphere over the United States. *Geophysical Research Letters*, *25*(10), 1709–1712. https://doi.org/10.1029/98GL00041

Jaegle, L., Jacob, D. J., Wennberg, P. O., Spivakovsky, C. M., Hanisco, T. F., Lanzendorf, E. J., … Wilson, J. C. (1997). Observed OH and HO_2 in the upper troposphere suggest a major source from convective injection of peroxides. *Geophysical Research Letters*, *24*(24), 3181–3184. https://doi.org/10.1029/97GL03004

Jenkin, M. E., Saunders, S. M., & Pilling, M. J. (1997). The tropospheric degradation of volatile organic compounds: A protocol for mechanism development. *Atmospheric Environment*, *31*(1), 81–104. https://doi.org/10.1016/s1352-2310(96)00105-7

Jenkin, M. E., Saunders, S. M., Wagner, V., & Pilling, M. J. (2003). Protocol for the development of the Master Chemical Mechanism, MCM v3 (Part B): Tropospheric degradation of aromatic volatile organic compounds. *Atmospheric Chemistry and Physics*, *3*(1), 181–193. https://doi.org/10.5194/acp-3-181-2003

Jenkin, M. E., Young, J. C., & Rickard, A. R. (2015). The MCM v3.3.1 degradation scheme for isoprene. *Atmospheric Chemistry and Physics*, *15*(20), 11,433–11,459. https://doi.org/10.5194/acp-15-11433-2015

Jöckel, P., Kerkweg, A., Pozzer, A., Sander, R., Tost, H., Riede, H., … Kern, B. (2010). Development cycle 2 of the Modular Earth Submodel System (MESSy2). *Geoscientific Model Development*, *3*(2), 717–752. https://doi.org/10.5194/gmd-3-717-2010

Jöckel, P., Tost, H., Pozzer, A., Kunze, M., Kirner, O., Brenninkmeijer, C. A. M., … Zahn, A. (2016). Earth System Chemistry integrated Modelling (ESCiMo) with the Modular Earth Submodel System (MESSy) version 2.51. *Geoscientific Model Development*, *9*(3), 1153–1200. https://doi.org/10.5194/gmd-9-1153-2016

Jones, N. B., Riedel, K., Allan, W., Wood, S., Palmer, P. I., Chance, K., & Notholt, J. (2009). Long-term tropospheric formaldehyde concentrations deduced from ground-based Fourier transform solar infrared measurements. *Atmospheric Chemistry and Physics*, *9*(18), 7131–7142. https://doi.org/10.5194/acp-9-7131-2009

Josse, B., Simon, P., & Peuch, V. H. (2004). Radon global simulations with the multiscale chemistry and transport model MOCAGE. *Tellus Series B: Chemical and Physical Meteorology*, *56*(4), 339–356. https://doi.org/10.1111/j.1600-0889.2004.00112.x

Kaiser, J., Wolfe, G. M., Bohn, B., Broch, S., Fuchs, H., Ganzeveld, L. N., … Keutsch, F. N. (2015). Evidence for an unidentified non-photochemical ground-level source of formaldehyde in the Po Valley with potential implications for ozone production. *Atmospheric Chemistry and Physics*, *15*(3), 1289–1298. https://doi.org/10.5194/acp-15-1289-2015

Lamarque, J. F., Emmons, L. K., Hess, P. G., Kinnison, D. E., Tilmes, S., Vitt, F., … Tyndall, G. K. (2012). CAM-chem: Description and evaluation of interactive atmospheric chemistry in the Community Earth System Model. *Geoscientific Model Development*, *5*(2), 369–411. https://doi.org/10.5194/gmd-5-369-2012

Le Breton, M., Bannan, T. J., Shallcross, D. E., Khan, M. A., Evans, M. J., Lee, J., … Percival, C. J. (2017). Enhanced ozone loss by active inorganic bromine chemistry in the tropical troposphere. *Atmospheric Environment*, *155*, 21–28. https://doi.org/10.1016/j.atmosenv.2017.02.003

Li, C., Joiner, J., Krotkov, N. A., & Dunlap, L. (2015). A new method for global retrievals of HCHO total columns from the Suomi National Polar-Orbiting Partnership Ozone Mapping and Profiler Suite. *Geophysical Research Letters*, *42*(7), 2515–2522. https://doi.org/10.1002/2015GL063204

Liao, J., Huey, L. G., Tanner, D. J., Flocke, F. M., Orlando, J. J., Neuman, J. A., … Stephens, C. R. (2012). Observations of inorganic bromine (HOBr, BrO, and Br2) speciation at Barrow, Alaska, in spring 2009. *Journal of Geophysical Research*, *117*, D00R16. https://doi.org/10.1029/2011JD016641

Lipari, F., & Swarin, S. J. (1982). Determination of formaldehyde and other aldehydes in autmobile exhaust with an improved 2,4-dinitrophenylhydrazine method. *Journal of Chromatography*, *247*(2), 297–306. https://doi.org/10.1016/s0021-9673(00)85953-1

Mahajan, A. S., Whalley, L. K., Kozlova, E., Oetjen, H., Mendez, L., Furneaux, K. L., … Saiz-Lopez, A. (2010). DOAS observations of formaldehyde and its impact on the HO_x balance in the tropical Atlantic marine boundary layer. *Journal of Atmospheric Chemistry*, *66*(3), 167–178. https://doi.org/10.1007/s10874-011-9200-7

Marbach, T., Beirle, S., Platt, U., Hoor, P., Wittrock, F., Richter, A., … Wagner, T. (2009). Satellite measurements of formaldehyde linked to shipping emissions. *Atmospheric Chemistry and Physics*, *9*(21), 8223–8234. https://doi.org/10.5194/acp-9-8223-2009

Meinshausen, M., Smith, S. J., Calvin, K., Daniel, J. S., Kainuma, M. L. T., Lamarque, J.-F., … van Vuuren, D. P. P. (2011). The RCP greenhouse gas concentrations and their extensions from 1765 to 2300. *Climatic Change*, *109*(1-2), 213–241. https://doi.org/10.1007/s10584-011-0156-z

Millet, D. B., Guenther, A., Siegel, D. A., Nelson, N. B., Singh, H. B., de Gouw, J. A., … Barkley, M. (2010). Global atmospheric budget of acetaldehyde: 3-D model analysis and constraints from in-situ and satellite observations. *Atmospheric Chemistry and Physics*, *10*(7), 3405–3425. https://doi.org/10.5194/acp-10-3405-2010

Millet, D. B., Jacob, D. J., Turquety, S., Hudman, R. C., Wu, S., Fried, A., … Clarke, A. D. (2006). Formaldehyde distribution over North America: Implications for satellite retrievals of formaldehyde columns and isoprene emission. *Journal of Geophysical Research*, *111*, D24S02. https://doi.org/10.1029/2005JD006853

Morgenstern, O., Hegglin, M. I., Rozanov, E., O'Connor, F. M., Abraham, N. L., Akiyoshi, H., … Zeng, G. (2017). Review of the global models used within phase 1 of the Chemistry–Climate Model Initiative (CCMI). *Geoscientific Model Development*, *10*(2), 639–671. https://doi.org/10.5194/gmd-10-639-2017

Morgenstern, O., Zeng, G., Abraham, N. L., Telford, P. J., Braesicke, P., Pyle, J. A., … Johnson, C. E. (2013). Impacts of climate change, ozone recovery, and increasing methane on surface ozone and the tropospheric oxidizing capacity. *Journal of Geophysical Research*, *118*(2), 1028–1041. https://doi.org/10.1029/2012JD018382

Muller, J. F., Liu, Z., Nguyen, V. S., Stavrakou, T., Harvey, J. N., & Peeters, J. (2016). The reaction of methyl peroxy and hydroxyl radicals as a major source of atmospheric methanol. *Nature Communications*, *7*, 13213. https://doi.org/10.1038/ncomms13213

Nicely, J. M., Anderson, D. C., Canty, T. P., Salawitch, R. J., Wolfe, G. M., Apel, E. C., … Weinheimer, A. J. (2016). An observationally constrained evaluation of the oxidative capacity in the tropical western Pacific troposphere. *Journal of Geophysical Research: Atmospheres*, *121*, 7461–7488. https://doi.org/10.1002/2016JD025067

Oman, L. D., Douglass, A. R., Ziemke, J. R., Rodriguez, J. M., Waugh, D. W., & Nielsen, J. E. (2013). The ozone response to ENSO in Aura satellite measurements and a chemistry-climate simulation. *Journal of Geophysical Research: Atmospheres*, *118*, 965–976. https://doi.org/10.1029/2012JD018546

Palmer, P. I., Jacob, D. J., Fiore, A. M., Martin, R. V., Chance, K., & Kurosu, T. P. (2003). Mapping isoprene emissions over North America using formaldehyde column observations from space. *Journal of Geophysical Research*, *108*(D6), 4180. https://doi.org/10.1029/2002JD002153

Pan, L. L., Atlas, E. L., Salawitch, R. J., Honomichl, S. B., Bresch, J. F., Randel, W. J., … Wolfe, G. (2016). The Convective Transport of Active Species in the Tropics (CONTRAST) experiment. *Bulletin of the American Meteorological Society*, *98*(1), 106–128. https://doi.org/10.1175/BAMS-d-14-00272.1

Pan, L. L., Honomichl, S. B., Randel, W. J., Apel, E. C., Atlas, E. L., Beaton, S. P., … Weinheimer, A. J. (2015). Bimodal distribution of free tropospheric ozone over the tropical western Pacific revealed by airborne observations. *Geophysical Research Letters*, *42*, 7844–7851. https://doi.org/10.1002/2015GL065562

Pan, L. L., Randel, W. J., Gary, B. L., Mahoney, M. J., & Hintsa, E. J. (2004). Definitions and sharpness of the extratropical tropopause: A trace gas perspective. *Journal of Geophysical Research*, *109*, D23103. https://doi.org/10.1029/2004JD004982

Parrish, D. D., Ryerson, T. B., Mellqvist, J., Johansson, J., Fried, A., Richter, D., … Herndon, S. C. (2012). Primary and secondary sources of formaldehyde in urban atmospheres: Houston Texas region. *Atmospheric Chemistry and Physics*, *12*(7), 3273–3288. https://doi.org/10.5194/acp-12-3273-2012

Peters, E., Wittrock, F., Grossmann, K., Friess, U., Richter, A., & Burrows, J. P. (2012). Formaldehyde and nitrogen dioxide over the remote western Pacific Ocean: SCIAMACHY and GOME-2 validation using ship-based MAX-DOAS observations. *Atmospheric Chemistry and Physics*, *12*(22), 11,179–11,197. https://doi.org/10.5194/acp-12-11179-2012

Petropavlovskikh, I., Shetter, R., Hall, S., Ullmann, K., & Bhartia, P. K. (2007). Algorithm for the charge-coupled-device scanning actinic flux spectroradiometer ozone retrieval in support of the Aura satellite validation. *Journal of Applied Remote Sensing*, *1*(1), 013540. https://doi.org/10.1117/1.2802563

Prather, M. J., & Jacob, D. J. (1997). A persistent imbalance in HO_x and NO_x photochemistry of the upper troposphere driven by deep tropical convection. *Geophysical Research Letters*, *24*(24), 3189–3192. https://doi.org/10.1029/97GL03027

Ravetta, F., Jacob, D. J., Brune, W. H., Heikes, B. G., Anderson, B. E., Blake, D. R., … Talbot, R. W. (2001). Experimental evidence fo the importance of convected methylhydroperoxide as a source of hydrogen oxide (HO_x) radicals in the tropical upper troposphere. *Journal of Geophysical Research*, *106*(D23), 32,709–32,716. https://doi.org/10.1029/2001JD900009

Read, K. A., Carpenter, L. J., Arnold, S. R., Beale, R., Nightingale, P. D., Hopkins, J. R., … Pickering, S. J. (2012). Multiannual observations of acetone, methanol, and acetaldehyde in remote tropical atlantic air: Implications for atmospheric OVOC budgets and oxidative capacity. *Environmental Science & Technology*, *46*(20), 11,028–11,039. https://doi.org/10.1021/es302082p

Ridley, B. A., & Grahek, F. E. (1990). A small, low flow, high sensitivity reaction vessel for NO chemiluminesence detectors. *Journal of Atmospheric and Oceanic Technology*, *7*(2), 307–311. https://doi.org/10.1175/1520-0426(1990)007<0307:ASLFHS>2.0.CO;2

Ridley, B. A., Walega, J. G., Dye, J. E., & Grahek, F. E. (1994). Distributions of NO, NO_x, NO_y, and O_3 to 12-km altitude during the summer monsoon season over New Mexico. *Journal of Geophysical Research*, *99*(D12), 25,519–25,534. https://doi.org/10.1029/94JD02210

Saiz-Lopez, A., & Fernandez, R. P. (2016). On the formation of tropical rings of atomic halogens: Causes and implications. *Geophysical Research Letters*, *43*(6), 2928–2935. https://doi.org/10.1002/2015GL067608

Sander, R. (2015). Compilation of Henry's law constants (version 4.0) for water as solvent. *Atmospheric Chemistry and Physics*, *15*(8), 4399–4981. https://doi.org/10.5194/acp-15-4399-2015

Sander, R., Baumgaertner, A., Gromov, S., Harder, H., Jöckel, P., Kerkweg, A., … Xie, Z.-Q. (2011). The atmospheric chemistry box model CAABA/MECCA-3.0. *Geoscientific Model Development*, *4*(2), 373–380. https://doi.org/10.5194/gmd-4-373-2011

Saunders, S. M., Jenkin, M. E., Derwent, R. G., & Pilling, M. J. (2003). Protocol for the development of the Master Chemical Mechanism, MCM v3 (Part A): Tropospheric degradation of non-aromatic volatile organic compounds. *Atmospheric Chemistry and Physics*, *3*(1), 161–180. https://doi.org/10.5194/acp-3-161-2003

Scinocca, J. F., McFarlane, N. A., Lazare, M., Li, J., & Plummer, D. (2008). Technical note: The CCCma third generation AGCM and its extension into the middle atmosphere. *Atmospheric Chemistry and Physics*, *8*(23), 7055–7074. https://doi.org/10.5194/acp-8-7055-2008

Sherwen, T., Schmidt, J. A., Evans, M. J., Carpenter, L. J., Großmann, K., Eastham, S. D., … Ordóñez, C. (2016). Global impacts of tropospheric halogens (Cl, Br, I) on oxidants and composition in GEOS-Chem. *Atmospheric Chemistry and Physics*, *16*(18), 12,239–12,271. https://doi.org/10.5194/acp-16-12239-2016

Singh, H. B., Salas, L. J., Chatfield, R. B., Czech, E., Fried, A., Walega, J., … Fuelberg, H. (2004). Analysis of the atmospheric distribution, sources, and sinks of oxygenated volatile organic chemicals based on measurements over the Pacific during TRACE-P. *Journal of Geophysical Research*, *109*, D15S07. https://doi.org/10.1029/2003JD003883

Stein, A. F., Draxler, R. R., Rolph, G. D., Stunder, B. J. B., Cohen, M. D., & Ngan, F. (2015). NOAA's HYSPLIT atmospheric transport and dispersion modeling system. *Bulletin of the American Meteorological Society*, *96*(12), 2059–2077. https://doi.org/10.1175/bams-d-14-00110.1

Stenke, A., Schraner, M., Rozanov, E., Egorova, T., Luo, B., & Peter, T. (2013). The SOCOL version 3.0 chemistry–climate model: Description, evaluation, and implications from an advanced transport algorithm. *Geoscientific Model Development*, *6*(5), 1407–1427. https://doi.org/10.5194/gmd-6-1407-2013

Stickler, A., Fischer, H., Williams, J., de Reus, M., Sander, R., Lawrence, M. G., … Lelieveld, J. (2006). Influence of summertime deep convection on formaldehyde in the middle and upper troposphere over Europe. *Journal of Geophysical Research*, *111*, D14308. https://doi.org/10.1029/2005JD007001

Still, T. J., Al-Haider, S., Seakins, P. W., Sommariva, R., Stanton, J. C., Mills, G., & Penkett, S. A. (2006). Ambient formaldehyde measurements made at a remote marine boundary layer site during the NAMBLEX campaign—A comparison of data from chromatographic and modified Hantzsch techniques. *Atmospheric Chemistry and Physics*, *6*(9), 2711–2726. https://doi.org/10.5194/acp-6-2711-2006

Tabazadeh, A., Yokelson, R. J., Singh, H. B., Hobbs, P. V., Crawford, J. H., & Iraci, L. T. (2004). Heterogeneous chemistry involving methanol in tropospheric clouds. *Geophysical Research Letters*, *31*, L06114. https://doi.org/10.1029/2003GL018775

Thompson, A. M. (1980). Wet and dry removal of tropospheric formaldehyde at a coastal site. *Tellus*, *32*(4), 376–383.
Tilmes, S., Lamarque, J.-F., Emmons, L. K., Kinnison, D. E., Ma, P.-L., Liu, X., … Val Martin, M. (2015). Description and evaluation of tropospheric chemistry and aerosols in the Community Earth System Model (CESM1.2). *Geoscientific Model Development*, *8*(5), 1395–1426. https://doi.org/10.5194/gmd-8-1395-2015
Tilmes, S., Lamarque, J. F., Emmons, L. K., Kinnison, D. E., Marsh, D., Garcia, R. R., … Blake, N. (2016). Representation of the Community Earth System Model (CESM1) CAM4-chem within the Chemistry-Climate Model Initiative (CCMI). *Geoscientific Model Development*, *9*(5), 1,853–1,890. https://doi.org/10.5194/gmd-9-1853-2016
Tost, H., Jockel, P., Kerkweg, A., Pozzer, A., Sander, R., & Lelieveld, J. (2007). Global cloud and precipitation chemistry and wet deposition: Tropospheric model simulations with ECHAM5/MESSy1. *Atmospheric Chemistry and Physics*, *7*(10), 2733–2757. https://doi.org/10.5194/acp-7-2733-2007
van Vuuren, D. P., Edmonds, J., Kainuma, M., Riahi, K., Thomson, A., Hibbard, K., … Rose, S. K. (2011). The representative concentration pathways: An overview. *Climatic Change*, *109*(1–2), 5–31. https://doi.org/10.1007/s10584-011-0148-z
Vigouroux, C., Hendrick, F., Stavrakou, T., Dils, B., De Smedt, I., Hermans, C., … De Mazière, M. (2009). Ground-based FTIR and MAX-DOAS observations of formaldehyde at Reunion Island and comparisons with satellite and model data. *Atmospheric Chemistry and Physics*, *9*(24), 9523–9544. https://doi.org/10.5194/acp-9-9523-2009
Volkamer, R., Baidar, S., Campos, T. L., Coburn, S., DiGangi, J. P., Dix, B., … Romashkin, P. A. (2015). Aircraft measurements of BrO, IO, glyoxal, NO_2, H_2O, O_2-O_2 and aerosol extinction profiles in the tropics: Comparison with aircraft-/ship-based in situ and lidar measurements. *Atmospheric Measurement Techniques*, *8*(5), 2121–2148. https://doi.org/10.5194/amt-8-2121-2015
Volkamer, R., Sheehy, P., Molina, L. T., & Molina, M. J. (2010). Oxidative capacity of the Mexico City atmosphere—Part 1: A radical source perspective. *Atmospheric Chemistry and Physics*, *10*(14), 6969–6991. https://doi.org/10.5194/acp-10-6969-2010
Wagner, V., von Glasow, R., Fischer, H., & Crutzen, P. J. (2002). Are CH_2O measurements in the marine boundary layer suitable for testing the current understanding of CH_4 photooxidation?: A model study. *Journal of Geophysical Research*, *107*(D3), 4029. https://doi.org/10.1029/2001JD000722
Watanabe, S., Hajima, T., Sudo, K., Nagashima, T., Takemura, T., Okajima, H., … Kawamiya, M. (2011). MIROC-ESM 2010: Model description and basic results of CMIP5-20c3m experiments. *Geoscientific Model Development*, *4*(4), 845–872. https://doi.org/10.5194/gmd-4-845-2011
Weibring, P., Richter, D., Fried, A., Walega, J. G., & Dyroff, C. (2006). Ultra-high-precision mid-IR spectrometer II: System description and spectroscopic performance. *Applied Physics B*, *85*(2-3), 207–218. https://doi.org/10.1007/s00340-006-2300-4
Weibring, P., Richter, D., Walega, J. G., & Fried, A. (2007). First demonstration of a high performance difference frequency spectrometer on airborne platforms. *Optics Express*, *15*(21), 13,476–13,495. https://doi.org/10.1364/OE.15.013476
Whalley, L. K., Goddard, A., Lee, J. D., Mahajan, A., Oetjen, H., Read, K. A., … Heard, D. E. (2010). The chemistry of OH and HO_2 radicals in the boundary layer over the tropical Atlantic Ocean. *Atmospheric Chemistry and Physics*, *10*(4), 1555–1576. https://doi.org/10.5194/acp-10-1555-2010
Wiedinmyer, C., Akagi, S. K., Yokelson, R. J., Emmons, L. K., Al-Saadi, J. A., Orlando, J. J., & Soja, A. J. (2011). The Fire INventory from NCAR (FINN): A high resolution global model to estimate the emissions from open burning. *Geoscientific Model Development*, *4*(3), 625–641. https://doi.org/10.5194/gmd-4-625-2011
Wolfe, G. M., Kaiser, J., Hanisco, T. F., Keutsch, F. N., de Gouw, J. A., Gilman, J. B., … Warneke, C. (2016). Formaldehyde production from isoprene oxidation across NO_x regimes. *Atmospheric Chemistry and Physics*, *16*(4), 2597–2610. https://doi.org/10.5194/acp-16-2597-2016
Wolfe, G. M., Marvin, M. R., Roberts, S. J., Travis, K. R., & Liao, J. (2016). The Framework for 0-D Atmospheric Modeling (F0AM) v3.1. *Geoscientific Model Development*, *9*(9), 3309–3319. https://doi.org/10.5194/gmd-9-3309-2016
Zeng, G., Williams, J. E., Fisher, J. A., Emmons, L. K., Jones, N. B., Morgenstern, O., … Griffith, D. W. T. (2015). Multi-model simulation of CO and HCHO in the Southern Hemisphere: Comparison with observations and impact of biogenic emissions. *Atmospheric Chemistry and Physics*, *15*(13), 7217–7245. https://doi.org/10.5194/acp-15-7217-2015
Zhou, X. L., & Mopper, K. (1997). Photochemical production of low-molecular-weight carbonyl compounds in seawater and surface microlayer and their air-sea exchange. *Marine Chemistry*, *56*(3–4), 201–213. https://doi.org/10.1016/s0304-4203(96)00076-x
Zondlo, M. A., Paige, M. E., Massick, S. M., & Silver, J. A. (2010). Vertical cavity laser hygrometer for the National Science Foundation Gulfstream-V aircraft. *Journal of Geophysical Research*, *115*, D20309. https://doi.org/10.1029/2010JD014445